TALLINN UNIVERSITY OF TECHNOLOGY
SCHOOL OF ENGINEERING
Department of Materials and Environmental Technology

STUDY OF STRUCTURAL DISORDER IN Cu_2ZnSnS_4 MONOGRAIN POWDERS BY RTPL AND RAMAN SPECTROSCOPY

Cu_2ZnSnS_4 KRISTALLVÕRE KORRASTAMATUSE UURIMINE TOATEMPERATUURSE FOTOLUMINESTSENTSI JA RAMAN SPEKTOSKOOPIA ABIL

MASTER THESIS

Student: Samuel Kanarbik

Student code: 212028KAYM

Supervisor: Dr. Marit Kauk-Kuusik,
Tenured associated professor,
Head of the Laboratory of
Photovoltaic Materials

Tallinn, 2024

AUTHOR'S DECLARATION

Hereby I declare, that I have written this thesis independently.
No academic degree has been applied for based on this material. All works, major viewpoints and data of the other authors used in this thesis have been referenced.

"....." 2024

Author: Samuel Kanarbik
/signature /

Thesis is in accordance with terms and requirements

"....." 2024

Supervisor: Marit Kauk-Kuusik
/signature/

Accepted for defence

"....."..... 2024

Chairman of theses defence commission: .....
/name and signature/

Non-exclusive licence for reproduction and publication of a graduation thesis[1]

I, Samuel Kanarbik, (author's name)

1. grant Tallinn University of Technology free licence (non-exclusive licence) for my thesis

"Study of structural disorder in Cu_2ZnSnS_4 monograin powders by RTPL and Raman spectroscopy"

(*title of the graduation thesis*)

supervised by Dr. Marit Kauk-Kuusik,

(*supervisor's name*)

1.1 to be reproduced for the purposes of preservation and electronic publication of the graduation thesis, incl. to be entered in the digital collection of the library of Tallinn University of Technology until expiry of the term of copyright.

1.2 to be published via the web of Tallinn University of Technology, incl. to be entered in the digital collection of the library of Tallinn University of Technology until expiry of the term of copyright.

2. I am aware that the author also retains the rights specified in clause 1 of the non-exclusive licence.

3. I confirm that granting the non-exclusive licence does not infringe other persons' intellectual property rights, the rights arising from the Personal Data Protection Act or rights arising from other legislation.

_____ (date)

[1] *The non-exclusive licence is not valid during the validity of access restriction indicated in the student's application for restriction on access to the graduation thesis that has been signed by the school's dean, except in case of the university's right to reproduce the thesis for preservation purposes only. If a graduation thesis is based on the joint creative activity of two or more persons and the co-author(s) has/have not granted, by the set deadline, the student defending his/her graduation thesis consent to reproduce and publish the graduation thesis in compliance with clauses 1.1 and 1.2 of the non-exclusive licence, the non-exclusive license shall not be valid for the period.*

TalTech Department of Material and Environmental technology

THESIS TASK

Student: Samuel Kanarbik, 212028KAYM

Study programme: KAYM, Materials and processes in sustainable energetics

Main speciality: Materials in sustainable energetics

Supervisor: Head of the Photovoltaic Materials laboratory, Dr. Marit Kauk-Kuusik, 5568 8092

Thesis topic:

(in English) Study of structural disorder in Cu_2ZnSnS_4 monograin powders by RTPL and Raman spectroscopy

(in Estonian) Cu_2ZnSnS_4 kristallvõre korrastamatuse uurimine toatemperatuurse fotoluminestsentsi ja Raman spektroskoopia abil

Thesis main objectives:

1. Investigating the impact of the Cu-Zn disordering within the CZTS crystal lattice on its structural and optical properties.
2. Exploring the correlation between room temperature photoluminescence (RTPL) and the performance characteristics of CZTS monograin layer solar cells.

Thesis tasks and time schedule:

No	Task description	Deadline
1.	Post-deposition annealing of the samples	January 2024
2.	Measurements of RTPL and Raman spectroscopy and IV characteristics	February 2024
3.	Analysis of obtained data	March-April 2024
4.	Writing the master's thesis	May 2024

Language: English

Deadline for submission of thesis: 23.05.2024

Student: Samuel Kanarbik ..... "....." 2024

/signature/

Supervisor: Dr. Marit Kauk-Kuusik .....".....".....2024

/signature/

Head of study programme: Dr. Sergei Bereznev .....".....".....2024

/signature/

Terms of thesis closed defence and/or restricted access conditions to be formulated on the reverse side

CONTENTS

PREFACE

This master's thesis has been completed in collaboration with the Laboratory of Photovoltaic Materials of TalTech, where the essential primary data for this work was collected. The topic of the thesis was initiated by the head of the laboratory, Dr. Marit Kauk-Kuusik.

In addition to my supervisor, the completion of this work was assisted by other staff of the laboratory, among whom I would like to express special thanks to senior researcher Dr. Maris Pilvet, under whose guidance the monograin layer solar cells were produced and *IV*-curves measured.

I would also like to separately thank my supervisor, Dr. Marit Kauk-Kuusik, without whom the completion of my thesis would have been very difficult, if not impossible. I express my sincere gratitude to Dr. Marit Kauk-Kuusik, who inspired, supported, and assisted me throughout the thesis.

In this thesis, disordering of the kesterite structure CZTS monograins was studied, using Raman spectroscopy and room-temperature photoluminescence measurements. The task was to employ different annealing temperatures to achieve different degrees of disordering in the Cu_2ZnSnS_4 crystals. Then monograin layer solar cells were produced to understand the effect of disordering on the output parameters of solar cells.

This project has received funding from the European Union's Horizon 2020 research and innovation programme under grant agreement No 952982 – CUSTOM-ARt. This work was also supported by ERDF projects TK210 and NAMUR+ (2020.4.01.16-0123), and by the Estonian Research Council grant PRG1023.

Keywords: Kesterites, photoluminescence, Raman spectroscopy, solar cells, master thesis

List of abbreviations and symbols

4N purity – purity of 99.99%

CBD – chemical bath deposition

CIGS – $Cu(In, Ga)S_2$

CZTS – Cu_2ZnSnS_4

DSSCs – dye sensitized solar cells

E_C – conduction band

E_f – Fermi level

e–field – electric field

E_g – band gap

E_V – valence band

FF – fill factor

FWHM – full width at half maximum

IEA - International Energy Agency

I_{MP} – maximum point of current

I_{SC} – short-circuit current

i–ZnO – (*intrinsic*) self-conducting (high resistance) ZnO

J_{SC} – short-circuit current density

MGL – monograin layer

PCE – power conversion efficiency

PL – photoluminescence

PMCA – primitive-mixed CuAu

PV – photovoltaic

qV_b – electronic charge of built–in potential

RTPL – room-temperature photoluminescence

S – degree of order

S_0 – ground state of order in a material

S_{eqm} – equilibrium amount of order

T_{ann} – annealing temperature

T_{cool} – cooling temperature

V_{MP} – maximum point of voltage

V_{OC} – open-circuit voltage

ZnO:Al – ZnO doped with Al

INTRODUCTION

In today's world, with a growing population and increasing global energy needs, it's essential for humanity to consider alternative energy sources alongside traditional ones. The decline in global fossil fuel reserves, coupled with population growth, emphasizes the importance of transitioning towards renewable energy sources like solar and wind power, as well as other options such as nuclear and hydroelectric energy.

Renewable energy is both economically and environmentally advantageous compared to widely used fossil fuels. The European Union's ambitious European Green Deal [1] aims to make Europe the first climate-neutral continent by 2050, with significant changes expected in the energy sector, particularly a transition to renewable sources like solar energy. Developing ecologically friendly, efficient, and versatile technologies is crucial to meet the necessary capacity for solar electricity production, complementing existing silicon solar panels [2].

Solar power offers a clean energy solution that can be swiftly and conveniently implemented to meet local energy needs. It is expected to play a central role in the future electricity grid, alongside wind power, potentially accounting for nearly 70% of global electricity generation by 2050. According to the International Energy Agency (IEA), the latest advancements in solar technology have made it the most economically viable source of electricity ever [3].

Solar cells operate on the principle of the photoelectric effect, requiring light for energy production. The absorber material within a solar cell must efficiently absorb light across the solar radiation spectrum, ideally with a high absorption coefficient, allowing for thinner absorber layers. Modern thin-film solar cells, like those using cadmium telluride (CdTe) and copper indium gallium selenide (CIGS), offer flexibility in manufacturing and application.

However, challenges remain, including the scarcity of certain materials and concerns over toxicity and usage restrictions. Exploring alternative absorber materials for thin-film solar cells, such as copper zinc tin sulphide (CZTS) and antimony selenide, is necessary. Comprised of abundant elements, these materials offer promising solutions for next generation photovoltaic applications.

Currently, CZTS-based solar cells hold the record for highest power conversion efficiency (PCE) among emerging inorganic thin-film PV candidates. Despite this, kesterite solar cells' PCE still falls significantly behind the theoretical maximum efficiency due to the large V_{OC} deficit.

Several factors contribute to the loss of V_{OC} in CZTS-based solar cells, including: 1) challenges in achieving a uniform absorber composition, causing fluctuations in bandgap and reduced device performance; 2) Cu–Zn antisite defects, inducing electrostatic potential fluctuations and band tailing, thus reducing V_{OC} and 3) complex defect properties introduced by multivalent Sn, leading to high recombination rates, and decreased V_{OC}.

This study investigated the impact of the Cu-Zn disordering within the CZTS crystal lattice on its structural and optical properties. An innovative approach to sample preparation for analysis was employed, and statistical analysis was utilized to minimise the influence of crystal facet orientation. Furthermore, this research aimed to explore the correlation between room temperature photoluminescence (RTPL) and the performance characteristics of CZTS monograin layer solar cells. These solar cell samples were fabricated using monograin layer technology.

1 THEORY AND LITERATURE REVIEW

1.1 Fundamentals of solar cells

In 1839 a French Physicist, Alexandre Edmond Becquerel, discovered the photovoltaic effect. Through experiment with metal electrodes and electrolyte Becquerel discovered the increase in conduction with illumination, which was later described by Albert Einstein in 1904 [4]. The photovoltaic effect in solar cell systems means that two dissimilar materials in close contact start to produce electrical voltage due to incident light. The light gives energy to the atoms of the semiconductor, and thus some electrons are freed from their usual positions. Those free electrons can then cross the junction between the two materials, so there will be a negative charge and negative voltage at one side of the junction and other side of the junction is then left with holes in the crystal structure. This can be compared to a battery, where one electrode of a battery has a negative voltage as opposed to the other electrode. As long as incident light continues to give energy to free electrons in the material, the system generates voltage and current due to forementioned PV effect [5]. The first solar cell was put together in 1941 using silicon monocrystal. Then in 1951, germanium solar cells were made which resulted in a solar cell with 4.5% efficiency [4]. Since then, efficiencies have been increasing over time using different materials and structures [6], with the latest maximum solar cell efficiency achieved in 2022, where quadruple junction solar cell with 47.6% conversion efficiency was measured [7].

Solar cells are mainly categorised into three different generations. Main differences are the materials and technologies used in different generations. The first generation uses crystalline wafer technology, with silicon (mono- and polycrystalline) as the absorber. Silicon is one of the most widely used materials in PV technologies. Thin film technology is considered as the second generation, using amorphous silicon, CdTe and CIGS as the absorbers. In this generation the target was to minimise used material and cost of cells. Third generation technologies which are considered as emerging technologies, are mix of the two previous generation technologies, with emphasis on charge carrier mechanisms and using more complex multinary compounds (also CZTS, which is the focus of this paper). Additionally, third generation technologies include dye sensitized solar cells (DSSCs), organic and polymeric cells, perovskites, quantum dot cells and multi-junction cells. Some examples of achieved power conversion efficiencies of different generations are brought out in Figure 1.1. The graph

categorizes solar cell technologies as follows: first generation solar cells are marked with blue, second generation with green and third generation with red colour. Additionally, multijunction cells, which utilize more than one *p*-*n* junction or GaAs technologies, are marked with purple, but these technologies are not considered under any mentioned generations.

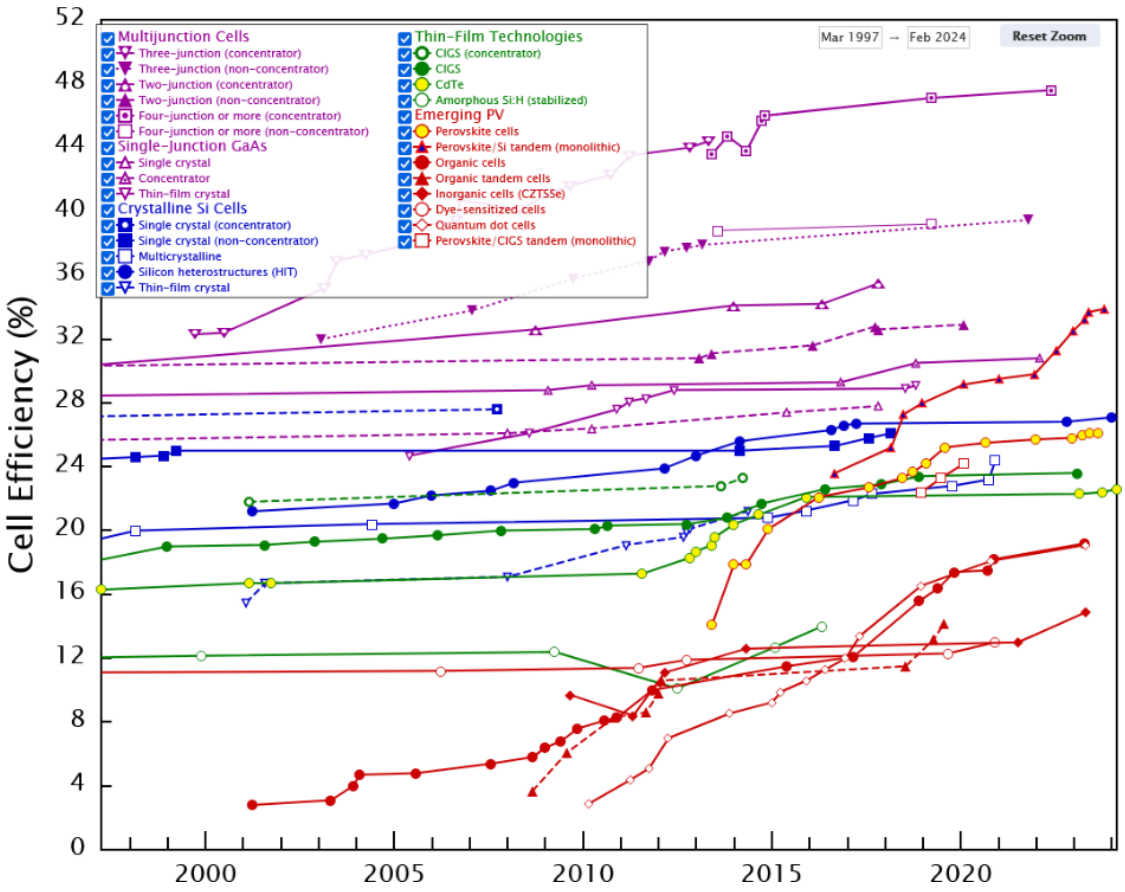

Figure 1.1. Examples of PV cell efficiencies [8].

Semiconductors are commonly employed in solar cell structures due to their adjustable electrical properties. Semiconductors are ideal for solar cell applications due to their intermediate electrical conductivity, lying between that of conductors like metals and insulators such as rubber. The conductivity of semiconductors is affected by various factors, including temperature, the use of dopants, illumination, and structure.

For semiconductors to be conductive, electrons must be able to cross the band gap (E_g). This band gap exists between the valence band and the conduction band, representing a region where electrons cannot present [9].

The wider the band gap, the harder it is for electrons to reach the conduction band. As can be seen on the Figure 1.2, there is no energy gap between conduction and valence band for conductors, which means that electrons can move freely and there is no need for extra energy to reach conduction band. For semiconductors the band gap is usually around 1-3 eV, just enough for electrons to be able to reach conduction band in excited state. In insulators, the band gap is too large for electrons to surpass it.

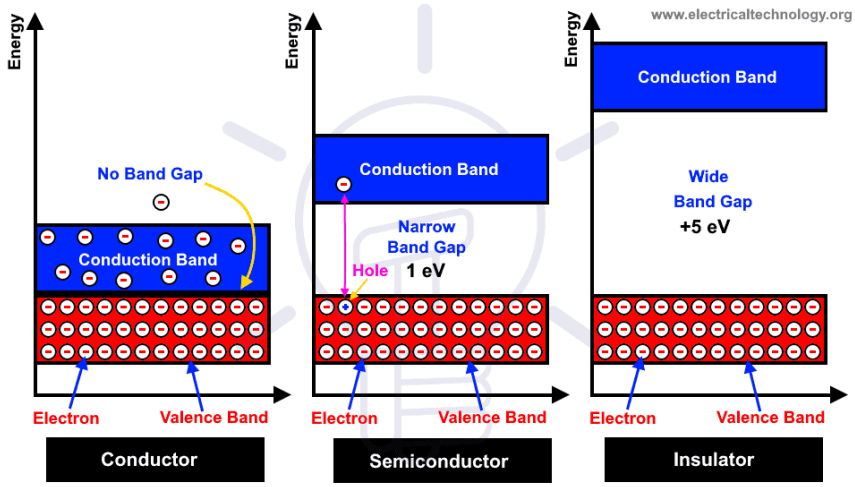

Figure 1.2. Band gap differences between different materials [10].

The junction essential for producing voltage and current is called the *p-n* junction. The main function of the *p-n* junction is the separation of electrons and holes, crucial for establishing the electron circuit. Electrons carry a negative charge, while holes are carrying the positive charge. The formation of the *p-n* junction between the two distinct semiconductors is driven by disparities in charge carrier concentrations. In *p*-type semiconductor, there is an excess of holes, while in a *n*-type semiconductor, there is an excess of electrons. This difference in holes and electrons concentrations, induces holes diffusion into regions of lower concentration and vice versa for electrons. The space where carriers diffuse forms an electric field known as the depletion region. (Figure 1.3a) The charge remains fixed in the depletion region and there are no mobile charge carriers in that zone. At the point where diffusion is balanced by drift current, thermal equilibrium is established and further diffusion is stopped and the Fermi levels for both semiconductors become equal (Figure 1.3 b) [11].

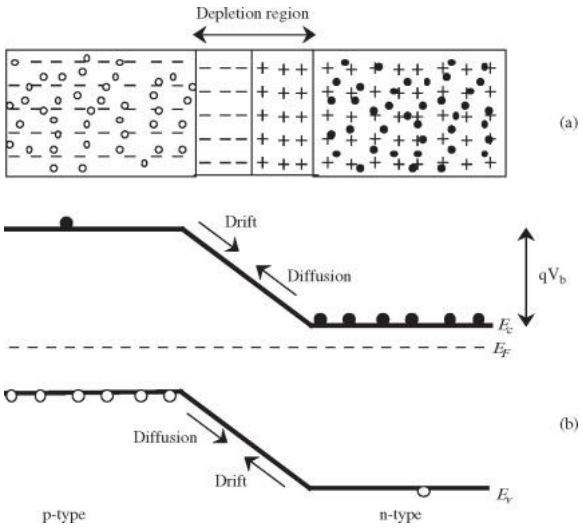

Figure 1.3 (a) Schematic structures of the *p-n* junction and (b) its energy band diagram in thermal equilibrium [11].

The initial stage in the operation of a functional solar cell involves the generation of electron-hole pair through the absorption of light photons. As mentioned above, the *p-n* junction helps to separate the electrons and holes, directing electrons towards the negative terminal and holes towards positive terminal, thereby generating electrical current (Figure 1.4) [12].

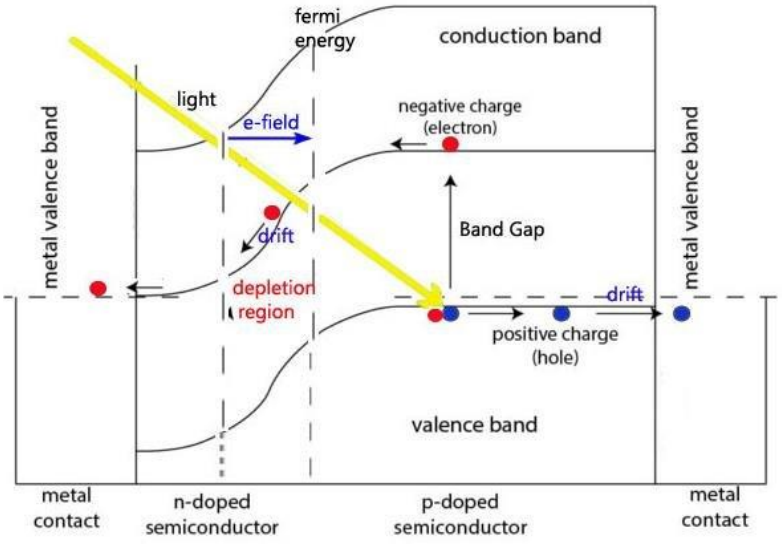

Figure 1.4 Working principle of a *p-n* junction solar cell [13].

1.2 Absorber material in solar cell structure

The main component within the solar cell structure (Figure 1.5) is the absorber layer. The primary task for the absorber layer is to absorb as much photons as possible. As previously mentioned, incident light excites electrons, allowing them to reach the conduction band and generate photocurrent. Absorber materials for solar cell structures are selected to align their bandgaps with regions of the solar spectrum exhibiting high photon flux, optimizing energy absorption [14].

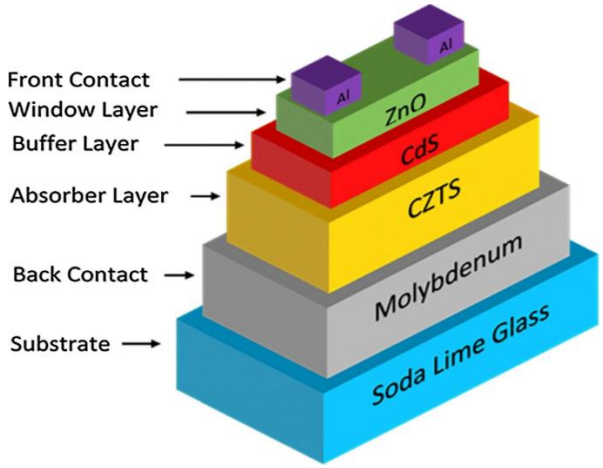

Figure 1.5. Structure example of CZTS solar cell [15].

Additionally, the absorption coefficient of the material within this layer must be as high as possible, ensuring that incident light is absorbed within a minimal thickness of the material. Consequently, less material is required to fabricate the absorber compared to materials with lower absorption coefficients. For example, when using silicon as the absorber layer, characterised by a low absorption coefficient, the layer thickness in a solar cell structure typically ranges from 150-200 micrometres. In modern thin film solar cells, the absorber layers can be considerably thinner, typically ranging from 1 to 5 micrometres, and sometimes even less. This reduction in thickness significantly reduces the amount of material required for the layer, consequently lowering the weight of the cells. Thin structure of the cells makes it possible to use them basically everywhere, including vehicles, buildings, and streetlights, due to their versatility and adaptability.

1.2.1 Properties of Cu_2ZnSnS_4

Today, the outlook for Cu_2ZnSnS_4-based (CZTS) thin film technology appears promising, as kesterite emerges as a highly favourable material for incorporation into solar cell structure as an absorber material. The elements that are used in kesterite are earth-abundant and non-toxic. CZTS has a *p*-type conductivity with direct band gap with an energy value of 1.5 eV, which can be tuned between 1-1.5 eV, by partially replacing S with Se. The absorption coefficient is $>10^4$ cm^{-1}. Besides that, in the field of emerging inorganic thin film technologies, CZTS has the highest measured power conversion efficiency (PCE) compared to other alternative materials [16]. So far the highest achieved PCE for kesterites is 14.9% [17]. There is definitely room for development, because the theoretical maximum for kesterites is around 30% according to the Shockley-Queissier limit [17].

CZTS crystallizes in three different types of tetragonal structures: kesterite, stannite and primitive-mixed CuAu (PMCA) structure. Kesterite CZTS is obtained from chalcopyrite type $CuInS_2$. In this derivation In atoms are substituted with Sn and Zn compared to stannite and PMCA structure, which are derived from CuAu-like structure [18]. The positioning of Cu and Zn atoms differ in kesterites and stannites, but Sn atoms stay in the same position for both structures. PMCA structure looks like a combination of two kesterite unit cells and one stannite unit cell. Kesterite structure is the most stable of the three. Today, it could be said that research focus more on the kesterite structure and less on stannite and PMCA structures.

Besides the different structures of CZTS, the synthesis of thin films may lead to different secondary phases such as ZnS, Cu_2SnS_3 and Cu_2S. This occurrence is attributed to the fact that CZTS can be obtained from relatively narrow region within the thermodynamic phase diagram. These mentioned phases can significantly influence device performance, as they may result in mismatches in crystal structure or band alignment, affecting the overall efficiency of the device. Also, the charge carrier transport and lifetime are negatively affected by the presence of crystallographic defects. For example, CdTe and CIGS exhibit minority carrier lifetimes 1-2 orders of magnitude longer than CZTS. This is due to the point defects, twinning, stacking faults, Cu-Zn disordering, and dislocations. When comparing CZTS to other chalcopyrite materials, lower efficiencies have been observed due to a low open-circuit voltage (V_{OC}). Studies indicate that this is primarily due to band gap fluctuations, which are caused by disordering of the Cu and Zn cations within the structure [19].

In crystal structures, defects are positions of the atoms, where the symmetry of the unit cell is disrupted, and the arrangement of atoms differs from the ideal crystal structure. As previously mentioned, some of them are extended defects (such as stacking faults, grain boundaries or dislocations). Point defects are defects that only involve one site of the structure. Figure 1.6 illustrates various types of point defects, such as antisites, interstitial atoms and vacancies. Interstitial atoms are defects where there is an atom in-between the lattice. Vacancies are defects where the atom is absent from its position and antisites are positions, where atoms have occupied a location of another element.

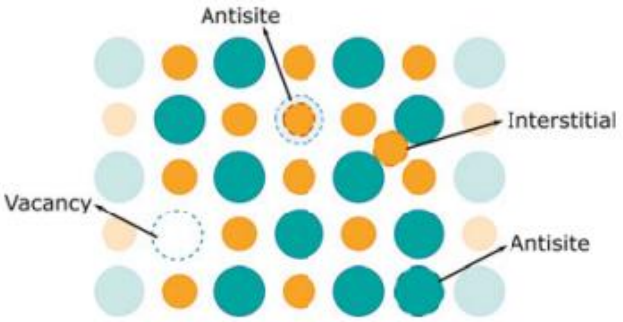

Figure 1.6 Illustration of intrinsic point defects in a crystal [20].

Cu_2ZnSnS_4 crystallises in the kesterite-type (space group *I4*) with four different cation sites being available in the structure [19]. In the ordered structure, Sn is positioned on site 2b, and one Cu is occupying the 2a position and the remaining is 2c, and Zn on 2d. Diffraction studies have shown partial or total disordering of Cu and Zn on the 2c and 2d positions (see Figure 1.7). Point defects of Cu_{Zn} and Zn_{Cu} require relatively low energy to form, so the disordering of Cu-Zn is highly probable in theory.

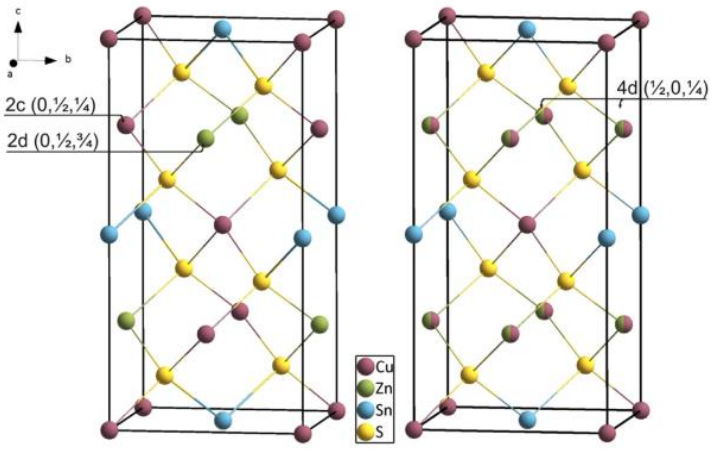

Figure 1.7 Unit cells of ordered (left) and disordered kesterite (right); sites involved in the order-disorder transition are labelled [19].

Studies [21] have shown that disordering is dependent on the cooling rate of sample synthesis, and the faster the cooling, the higher the degree of Cu-Zn disordering in the sample. Slow cooling is associated with more ordered CZTS [22]. When a material undergoes slow cooling, there's more time for defects and clusters within its structure to rearrange and relax into more stable configurations. These defects and clusters often have high formation energy, meaning it requires a significant input of energy to form them in the first place. Slow cooling allows this energy to be gradually dissipated, leading to a more thermodynamically favourable state.

However, when the cooling rate is fast, there isn't enough time for these defects and clusters to relax so they will stay in the structure [23].

Research has indicated that rapid cooling facilitates the randomisation of Cu and Zn atoms on the 2c and 2d sites within the structure, resulting in effective *I42m* space group. However, when samples are gradually cooled at a rate of 1 K/h, only about 30% of the Cu and Zn atoms exhibit disorder on the crystallographic sites. A 30% occurrence of disorder, leading to Cu-Zn antisite defects, could be indeed considered significant. Such defects are known to cause a 100 meV deviation in the band gap [24]. Raman spectroscopy has proven to be an effective method in distinguishing between ordered and disordered CZTS materials. In disordered CZTS, broader peaks with minimal shifts (~1-2 cm^{-1}) are observed. Raman studies have shown that the critical temperature for disordering is 260 °C, over that temperature pure sulphide-based kesterites become completely disordered at equilibrium [25].

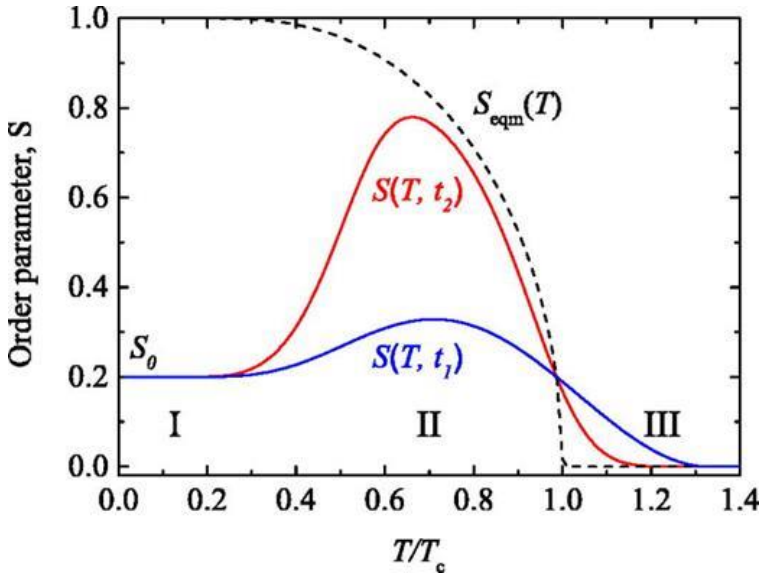

Figure 1.8 The degree of order (*S)* in a material having an order-disorder transition with critical temperature T_C [24].

Figure 1.8 shows a description of order-disorder transition in crystalline material, which was made by Bragg and Williams [26]. Usually, the ground state means that the structure is ordered and in equilibrium, but in this case the ordering parameter, S, shows how ordered is the material. When S is equal to 1, the material is perfectly ordered and when it is 0, the material is completely disordered. In the graph, the model of Vineyard has been used to calculate equilibrium amount of order against temperature, which is displayed with the dashed line. When temperature rises, S_{eqm} decreases, and the disordering is complete when the material reaches the point of critical temperature. The solid curves show two different annealing times ($t_2 > t_1$), with three different regimes. Regime I does not increase S significantly, II is enough for atomic motion, so S increases towards S_{eqm}. In regime III, which shows the reaction of the material over the critical temperature, it can be seen that ordering reduces below S_0, and material becomes completely disordered. In reality there can exist a practical upper limit on the level of order achievable within a reasonable timeframe [24].

Experiments have revealed that the V_{OC} of $Cu_2ZnSnSe_4$ and $Cu_2ZnSn(S, Se)_4$ can be improved through Cu-Zn ordering. However, the deficit of V_{OC} observed in kesterites remains significant. A direct connection has been found between anomalies in temperature treatment on the transport properties and the order-disorder transition for the kesterite. Consequently, this transition impacts the photovoltaic and thermoelectric properties of kesterite based devices [27].

Studies have revealed a difference in the band gap energy between ordered and disordered kesterite phases, with photoluminescence studies indicating a narrower energy gap between these structures [28]. The degree of disorder in CZTS can be affected by the speed of cooling after sample synthesis, rapid cooling tends to increase disorder, while slower cooling promotes a more ordered arrangement. Furthermore, the degree of Cu-Zn disorder can be adjusted by utilising various cooling methods or applying low-temperature post-annealing treatments.

A previous study [22] examined how the degree of Cu-Zn disordering in Cu_2ZnSnS_4 monograin powders affects the performance of CZTS-based monograin layer (MGL) solar cells. Different cooling and low-temperature annealing methods were used to adjust the ordering level, which was characterised using low temperature photoluminescence (PL) and Raman spectroscopy. The results showed that increased ordering increased the band gap energy of the CZTS material, leading to higher V_{OC} values in the corresponding MGL solar cells. (685 mV vs 759 mV).

1.3 Monograin layer technology

Monograin layer technology is a solar cell technology, where the absorber layer consists of monograin powders. The use of monograin technology means that the solar cells become cheaper in price and can achieve higher power conversion efficiencies, latter is because there are less grain boundaries compared to polycrystalline materials. This means that the layer absorbs light better, there are more charge carriers and less recombination of holes and electrons. Usually, the synthesis is done using the molten salt method, where micro-crystalline materials are grown, while controlling the chemical composition and doping concentration.

Cu_2ZnSnS_4 has been successfully synthesised in the form of monograin powders using LiI, NaI, KI, RbI and CsI as a flux material [29]. In another study, $Cu_2CdGeSe_4$ powder materials were synthesised in two different salts –CdI_2 and KI liquid phase [30]. Also, different research of $Cu(In_{1-x}Ga_x)Se_2$ monograin powders with different x values (x = 0 - 1) have been performed. This was done by using KI as a flux material in the liquid phase, as in current research. The binary precursor compounds CuSe, InSe, and Ga_2Se_3 were synthesised from elements with a purity of 4N in evacuated quartz ampoules [31]. In another research, $Cu_{10}Cd_2Sb_4S_{13}$ monograin powders were synthesised using the similar molten salt synthesis-growth method [32] like in this experiment.

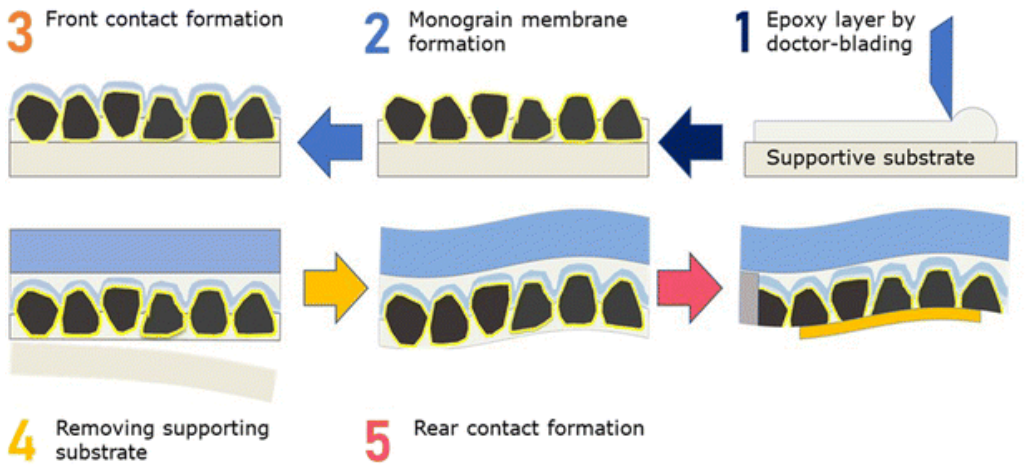

Figure 1.9 Monograin layer fabrication [16].

The monograin layer technology involves a complex multi-step process. The membrane fabrication process begins with a thin layer of low shrinkage polymer, into which previously

manufactured powder crystals covered with buffer layer are inserted. This means that photovoltaic functionality is already achieved in the monograin level, distinguishing it from other technologies. Subsequent processes include the formation of front contacts and rear contacts. (Figure 1.9) [16].

1.4 Summary of the literature review and aim of the study

The global energy demands continue to rise, driven by the rapid growth of the population each year. Meanwhile, worldwide reserves of fossil fuels are gradually diminishing and possibly starting to decline. These are the factors that are greatly affecting our ways of acquiring energy in the near future. As a community (of all people on Earth) we should focus even more to alternative energy sources. This is also supported by the fact that European Union has coordinated a Green Deal to develop Europe into being a climate neutral area for the year 2050.

I believe that every research effort aimed at developing green energy sources contribute to reaching our established goals. Utilising solar panels to generate electricity is definitely one of the ways to go. Of course, the field of thin film technologies offers plenty of opportunities for development, which is also the reason why I am dedicated to writing this thesis. Despite ongoing research into the development of various thin film materials, kesterites have not yet fully realized their potential. This is strong motivation for me to write my thesis on this topic. As research have shown, the properties of kesterite Cu_2ZnSnS_4 are theoretically excellent for its application as absorber layer in solar cell. This material is inexpensive, environmentally friendly, composed of earth abundant elements and possesses a satisfactory theoretical power conversion efficiency.

The aim of the study was to introduce different degree of disordering in Cu_2ZnSnS_4 powders by annealing them above the critical temperature (T_C=260 ^oC [24]) within the temperature range of 260 ^oC -950 ^oC. Subsequently, the crystal structure was rapidly quenched by cooling the material in ice water. The impact of the disordering degree within the CZTS crystal lattice on the structural and optical properties (room-temperature photoluminescence peak position, intensity and FHWM) was studied. Additionally, absorber powders with varying degrees of disorder were utilised in monograin layer solar cells and the photovoltaic parameters were examined.

Previously, it was believed that Raman spectroscopy was unsuitable for determining the ordering parameter in monograin powders due to the slight variations in Raman spectra caused by differently orientated crystal faces and polarization. However, in this study, a novel sample preparation methodology and statistical analysis were employed to mitigate the impact of crystal facet orientation.

2 EXPERIMENTAL

The monograin powders used in these experiments were previously synthesised at the Laboratory of Photovoltaic Materials of TalTech. Binary compounds of CuS, ZnS and SnS as precursors were used to produce high-purity Cu_2ZnSnS_4 monograin powders in KI molten salt in a sealed quartz ampoule. The fraction size of the powders used in this study was 56-75 micrometres. More detailed description of monograin powder synthesis is found elsewhere [30–32].

2.1 Post treatment of the Cu_2ZnSnS_4 powders

After the synthesis of the Cu_2ZnSnS_4 powders, all the samples were annealed isothermally in sealed quartz ampoules (Figure 2.1) at temperatures ranging from 260 to 950 °C for 15 minutes, followed by cooling through quenching into ice water. Annealing process was carried out in a Nabertherm muffle furnace (Figure 2.2). During the temperature treatment of the samples, particulary at higher temperatures, the walls of the ampoules began to fade. This phenomenon occurs because the material can partially decompose at temperature higher than 450 °C, and sulphur or Sn-S compounds becomes volatile.

Figure 2.1 Cu_2ZnSnS_4 powders sealed in quartz ampoules post anneal.

Figure 2.2 Nabertherm muffle furnace

In Table 2.1, the annealing temperatures and the corresponding cooling ice water temperature are presented. The powders were labeled according to their annealing temperatures (S260-S925). Powders S260-S500 and S900-S925 had a particle fraction size of 56-63 micrometres, while powders S525-S875 had particle fraction size of 63-75 micrometres.

Table 2.1 Powders with their annealing temperatures and corresponding cooling temperatures.

Object	T_{ann}, °C	T_{cool}, °C	**Object**	T_{ann}, °C	T_{cool}, °C
S260	260	2	S650	650	2
S300	300	2	S675	675	3
S340	340	2	S700	700	1
S380	380	2	S725	725	3
S420	420	2	S750	750	2
S460	460	2	S775	775	3
S500	500	2	S800	800	2
S525	525	2	S825	825	2
S550	550	2	S850	850	2
S575	575	2	S875	875	2
S600	600	2	S900	900	1
S625	625	2	S925	925	2

In this experiment, post-annealing was performed to express the effect of temperature treatment on the ordering of crystal structures and the output parameters of the produced cells.

2.2 Monograin layer solar cell preparation

After post-annealing process, the powders were used as absorber layers in miniature solar cells. The monograin layer solar cells were produced at Laboratory of Photovoltaic Materials of TalTech with the help of Dr. Maris Pilvet.

Prior to assembling the cells, a CdS buffer layer was deposited onto the monograins to form a *p*-*n* junction. This process was carried out using chemical bath deposition (CBD). CdS is a suitable buffer layer for its direct bandgap of 2.42 eV [33] and it is compatible with CZTS bandgap of ~1.5 eV. Buffer layer is needed to create a barrier to interrupt the recombination of charge carriers, electrons, and holes, as this would decrease the conductivity of the produced cells. For an effective solar cell, it is necessary to make sure the structure's semiconductors' energy band gaps are compatible with each other. Besides the optimum bandgap, CdS has good thermal and chemical stability [33], which is necessary for the buffer layer not to chemically react with absorber layer or window layer. This also contributes to the material not to degrade thermically or disintegration during the deposition of other layers. Since CdS has a direct bandgap, the material has strong optical absorption and that is also the reason for its use in solar cell structures. Materials with direct bandgaps absorb light significantly better than materials with an indirect bandgap.

To make a monograin membrane, a resin was initially mixed, into which the monograins were subsequently pressed. The resin consisted of EpoThin™ 2 epoxy hardener and EpoThin™ 2 epoxy resin, both from Buehler. This two-component resin consisted of epoxy resin and a hardener in a ratio of 1:0.45. After mixing the two components, a certain buffer time was required for the polymerisation of the material. Once the resin had reached an appropriate viscosity after hardening, a layer of the resin was applied with a correct thickness, typically dependent on the fraction of the grains used. Usually, the optimal thickness is about half the diameter of the used grains. The doctor blade employed in this process was the byko-drive XL Automatic Film Applicator by BYK, selected for its capability to achieve a uniform layer of resin (Figure 2.1). The epoxy was applied onto a supporting substrate, a transparent film (ISOPET OAN 125 µm). Prior to applying the layer of epoxy resin, both the transparent film and the vacuum board of the doctor blading device were cleaned with ethanol. This step is essential to ensure the absence of dust on the film, which could lead to an uneven epoxy layer.

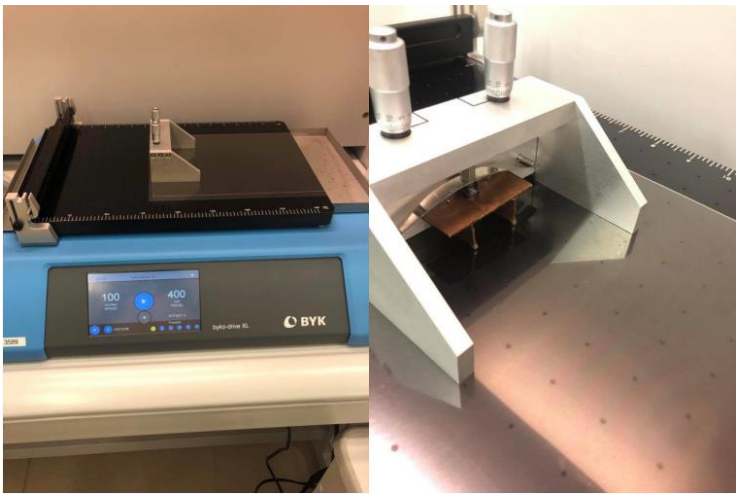

Figure 2.1 Doctor blading device used in the membrane preparation process.

After using the doctor blade to achieve the desired thickness of the epoxy film, it needed to harden for 2.5 hours before applying the powder. Then, the powder was carefully added to the epoxy layer to ensure the entire sample was covered with grains (Figure 2.2).

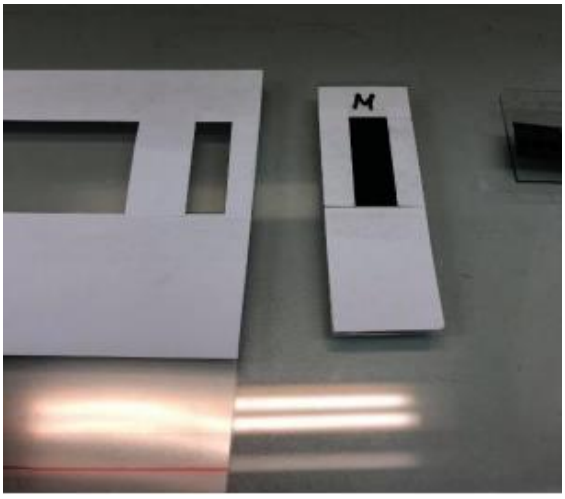

Figure 2.2 A sample with applied CZTS powder (right) and a clear sample of the epoxy resin (left).

Once all the samples had been covered with CZTS monograin powder, they were placed into a refrigerator to finalise the polymerisation process. Before depositing the ZnO window layer, the supporting papers around membranes were removed. The ZnO layer was deposited using an AJA International magnetron sputtering device, a commonly used high-vacuum method for depositing transparent conductive oxide thin films (Figure 2.3). ZnO layers are very often used as window layers in PV solar cell structures. The material to be used in this structure should exhibit a combination of high electrical conductivity and a low optical absorption coefficient

within the visible light spectrum [34]. In thin film solar cells structures based on absorber materials like CdTe or $CuIn(S, Se)_2$, RF-magnetron sputtering is commonly employed to deposit contact and window layers of zinc oxide (ZnO:Al and *i*-ZnO). Higher PCEs have been achieved when the sputtering process is conducted in a pure argon environment. Research has shown that depositing a conductive ZnO layer (ZnO:Al) in an oxygen-rich environment can have a detrimental effect on the open-circuit voltage of the solar cells [35].

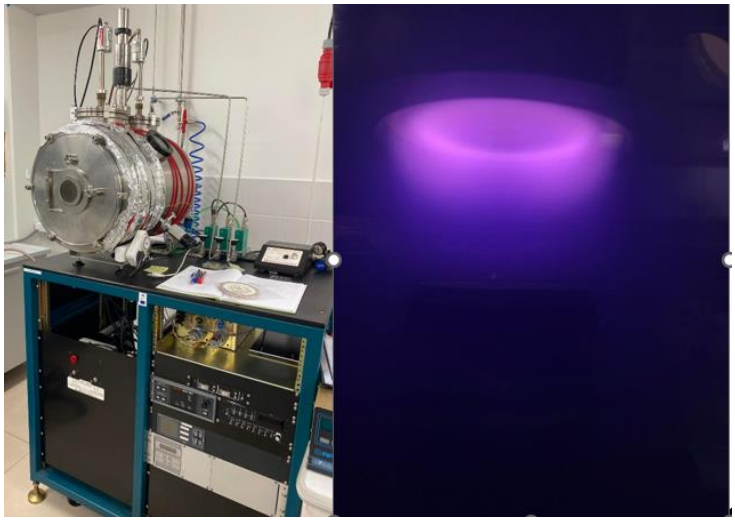

Figure 2.3 ZnO window layer deposition, sputtering device on the left and sputtering process on the right (argon plasma has a peculiar purple hue).

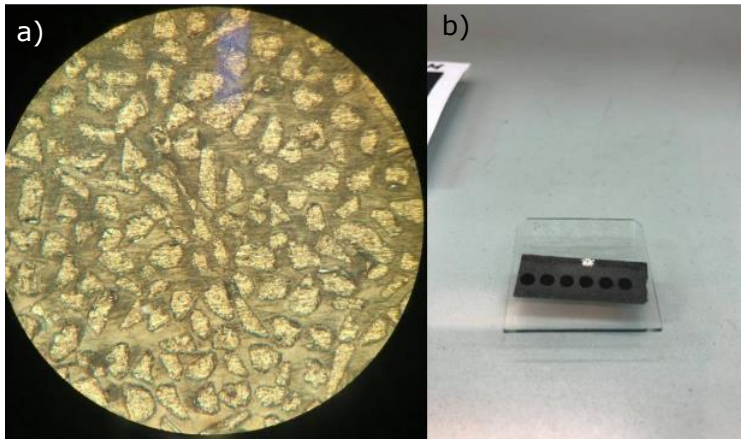

Figure 2.4 a) An optical microscope picture of the epoxy layer and the polished monograins of the absorber layer. b) Produced miniature solar cell.

Following the deposition of the window layer, silver paste containing Ag-nanorods was applied to the cells to improve the function of collector electrode. Finally, the samples were glued onto a glass substrate using the previously used epoxy resin and left to cure for ~12 hours.

Subsequently, the supporting substrate films on which the structures are based were removed. The entire solar cell structure- Ag-electrodes/ZnO window layer/CdS/CZTS monograin layer remained on the glass substrate. In the next process, the layer of the epoxy resin was etched with sulphuric acid until the top of the grains were visible under a microscope. Subsequently, the epoxy was manually polished to ensure that the grains were level with the epoxy (Fig. 2.4).

2.3 Characterisation methods

For room-temperature Raman spectroscopy and photoluminescence measurements, the powders were prepared onto a substrate in such a way that the flat facets of the monograins were accessible for measurements with the larger side facing upwards. The grains were poured onto a glass and then shaken, allowing them to roll over onto their larger facet. Next, a double-sided graphite tape was used to transfer the monograins from the glass onto a metal substrate (Figure 2.5).

Figure 2.5 An optical microscope picture of the measured monograins on the left and the samples S700-S950 with the reference sample in a holder.

2.3.1 Raman spectroscopy

Raman spectroscopy is a non-destructive analysis technique to acquire information on the structures, phases, crystallinity, and molecular bonds of various materials. The Raman effect was discovered in 1928 and is named after its discoverer, Krishan Raman. During the process of Raman spectroscopy, the effect that occurs is called the Raman effect, which is used for analysis of different materials. The Raman effect refers to the inelastic scattering of light caused by the interaction between light and the vibrations of molecules or crystal lattices within a substance. The principle is based on the idea that in the case of inelastic scattering of light, the wavelength and energy of the light beam changes. The intensity of the scattered light beam is recorded on the scale of Raman shift and intensity of the Raman spectrum. The Raman shift is the difference between the frequencies of the original radiation and the scattered radiation. Each material and substance have its own unique Raman spectrum, making it possible to study substances in gaseous, liquid, and solid states. Raman spectroscopy enables the identification of substances, evaluation of their crystallinity, determination of crystal structure, phase composition, intrinsic stress/strain, contamination, and impurity levels, as well as analysis of vibration modes. In this thesis, the Raman spectrometer HORIBA Jobin Yvon LabRam HR800 of the Laboratory of Photovoltaic Materials at TalTech (Figure 2.5) was used. A laser with a wavelength of 532 nanometres was used to excite the powders [36,37].

Figure 2.5 Raman spectrometer used in this research, HORIBA Jobin Yvon LabRam HR800.

2.3.2 Room-temperature photoluminescence

Room-temperature photoluminescence (RT-PL) was also measured by Horiba LabRam 800HR spectrometer of the Laboratory of Photovoltaic Materials at TalTech (Figure 2.5) using 532 nm laser for excitation. PL spectroscopy serves as a non-destructive method for investigating impurities, defects, and band gaps in semiconductors and other materials. The process of absorbing light, generating electron-hole pairs, and subsequent recombination provides valuable insights into the electronic structure of the material. The emitted photons during recombination carry information about the energy levels of the material's valence and conduction bands, allowing researchers to conclude important properties such as band gaps. This understanding is crucial for optimizing semiconductor materials for various technological applications, ranging from microelectronics to photovoltaics. Different parameters such as peak symmetry, full width at half maximum (FWHM) of the peak, centre position of the peak and fine structure are measured and studied to give information about the structures and composition of various semiconductors. Peak symmetry gives information about the homogeneity of the material (defects and variations in doping concentration). FWHM is used to understand the quality of the crystalline material and the distribution of defects. The broader FWHM can indicate the present of defects or inconsistencies in the structure. The centre position of the peak indicates the energy of the emitted photons, which is used to determine the band gap of the corresponding material.

Overall, PL spectroscopy stands as a vital technique for material scientists and engineers, enabling the precise characterisation and advancement of semiconductor materials [38,39].

2.3.3 Solar cell characteristics

To control the quality of the produced solar cells, it is necessary to measure the voltage-current characteristics, commonly known as the *IV*-curves of the solar cells (Figure 2.6).
The *IV*-curve is necessary to acquire the most important output parameters of a solar cell. These are the main parameters directly related to the functioning of the solar cells in an active working environment. The most important parameters are open-circuit voltage (V_{OC}), short-circuit current (I_{SC}), efficiency (η) and fill factor (*FF*). During the measurement of V_{OC}, there is zero load applied to the contacts of the cell, so the current throughout the structure is zero. In the case of the I_{SC} measurement, a load with zero resistance is connected to the solar cell and the voltage across the contacts is equal to zero. With V_{OC} and I_{SC}, it is possible to find out

the maximum voltage and current that can be obtained from a given cell. Fill factor provides information about the actual power loss of the solar cell (Equation 2.1). Maximum power point defines the maximum power output of the corresponding solar cell. Lastly, efficiency is the ratio between the maximum generated power of the solar cell and the power of the incident light (Equation 2.2) [40].

$$FF = \frac{V_{MP} \times I_{MP}}{V_{OC} \times I_{SC}} \times 100\% \quad (2.1)$$

where V_{MP} – voltage of maximum power (V);

I_{mp} – current of maximum power (A);

FF – fill factor (%);

V_{OC} – open-circuit voltage (V);

I_{SC} – short-circuit current (A)

$$\eta = \frac{V_{OC} \times I_{SC} \times FF}{P_{in}} \times 100\% \quad (2.2)$$

where V_{OC} – open-circuit voltage (V);

I_{SC} – short-circuit current (A);

FF – fill factor (%);

η - efficiency (%);

P_{in} – power of the incident light (100 mW/cm^2)

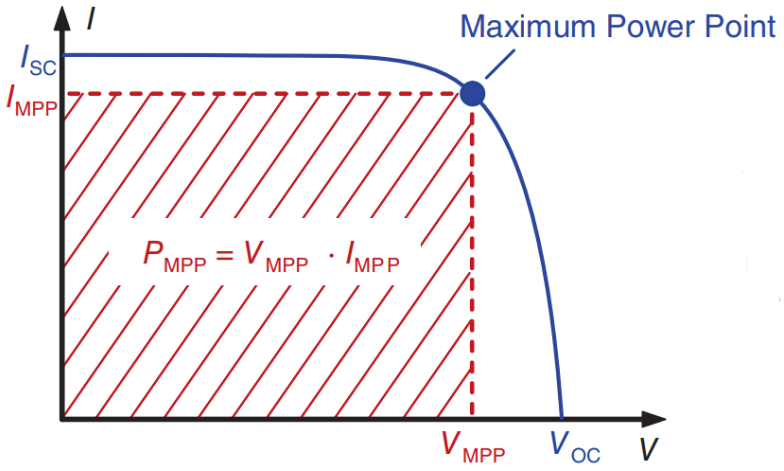

Figure 2.6. Characteristic curve of a solar cell [41].

In this work, current-voltage characteristics were measured using the computer-controlled bipolar power supply Keithley 2400. The power supply was controlled by the computer program IVCurve. In addition, we used a solar simulator Newport Class AAA, with a light power density of 100 mW/cm^2 on the sample surface and spectrally compatible with AM1.5G radiation.

3 RESULTS

3.1 Structural disordering study in CZTS by Raman spectroscopy

Room-temperature Raman spectroscopy was conducted on all samples, with each sample being measured on 10 different crystal facets. After that, average spectra for each sample were calculated using Origin 2015 and 2018. Subsequently, the average spectra were fitted using the Fityk program, employing Lorentzian function. Raman graphs are usually given in the units of wavenumbers (cm^{-1}), with intensity measured in arbitrary units. Figure 3.1 shows the Raman spectrum of reference CZTS powder (as grown).

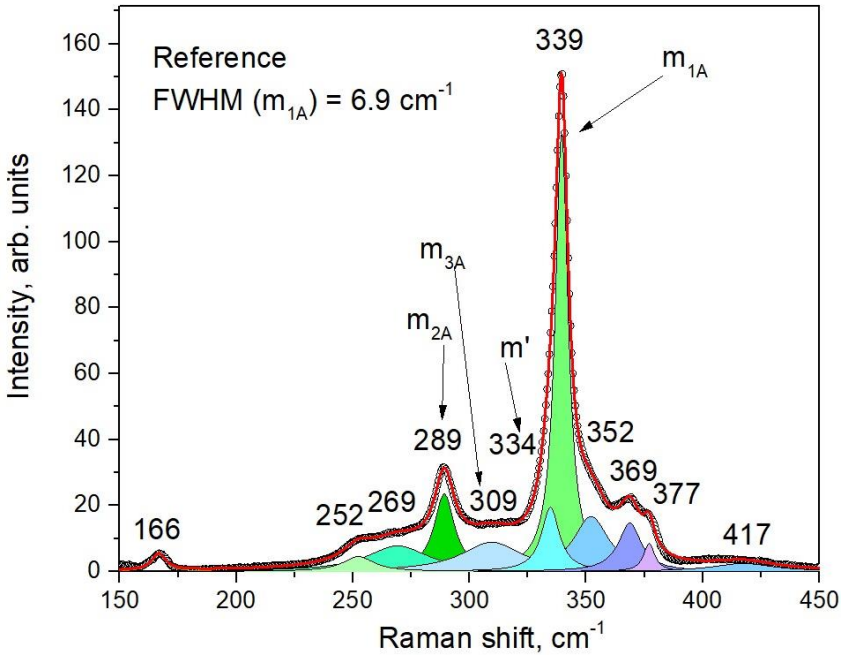

Figure 3.1 Raman spectra of the reference sample.

According to previous research and literature, the main peaks of kesterite CZTS in Raman spectroscopy should stand at 340, 284 and 273 cm^{-1}, with the peak at 340 cm^{-1} being the most intense [42]. The exact peak positions can have minimal differences due to different synthesis methods and the conditions of the synthesis. Also, in this experiment, it could be seen that not all the measured Raman main peaks are exactly at the same position, which could be seen on Figures 3.2 and 3.3. All the measured samples exhibit a main peak at 336-

338 cm^{-1} (Figure 3.2 and 3.3), which corresponds to CZTS kesterite structure. This can be attributed to the fact that the measurements were done on different days, and the calibration of the device was slightly different.

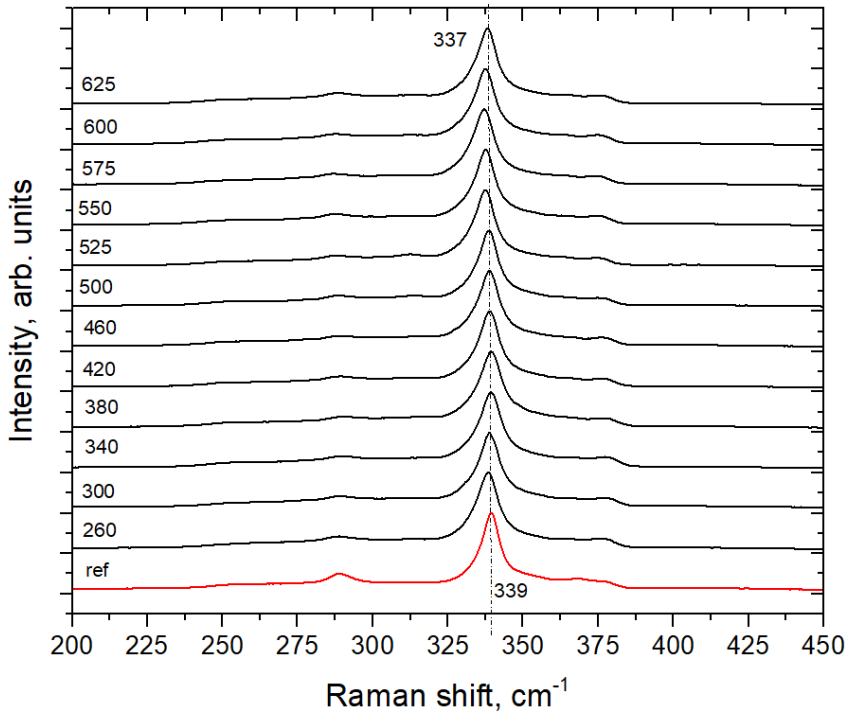

Figure 3.2. Room temperature Raman spectra of samples S260-S625 and the reference sample.

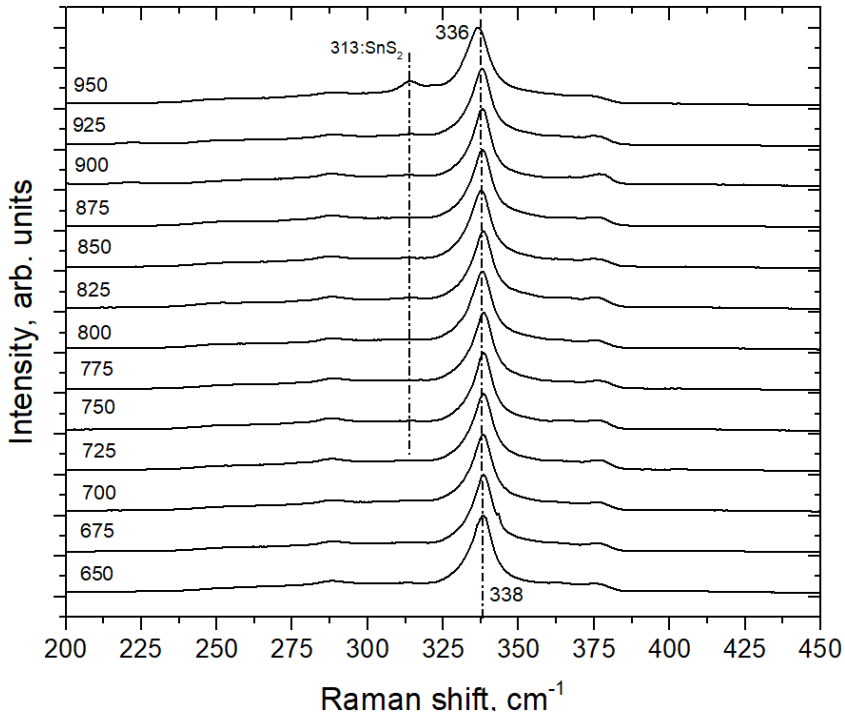

Figure 3.3. Room temperature Raman spectra of samples S650-S950.

When comparing the Raman spectrum of a reference sample to some samples subjected to higher annealing temperature, it could be noted that the A_1 peak in the Raman spectrum becomes broader (FWHM changed from 6.9 cm^{-1} to ~9.2 cm^{-1}).

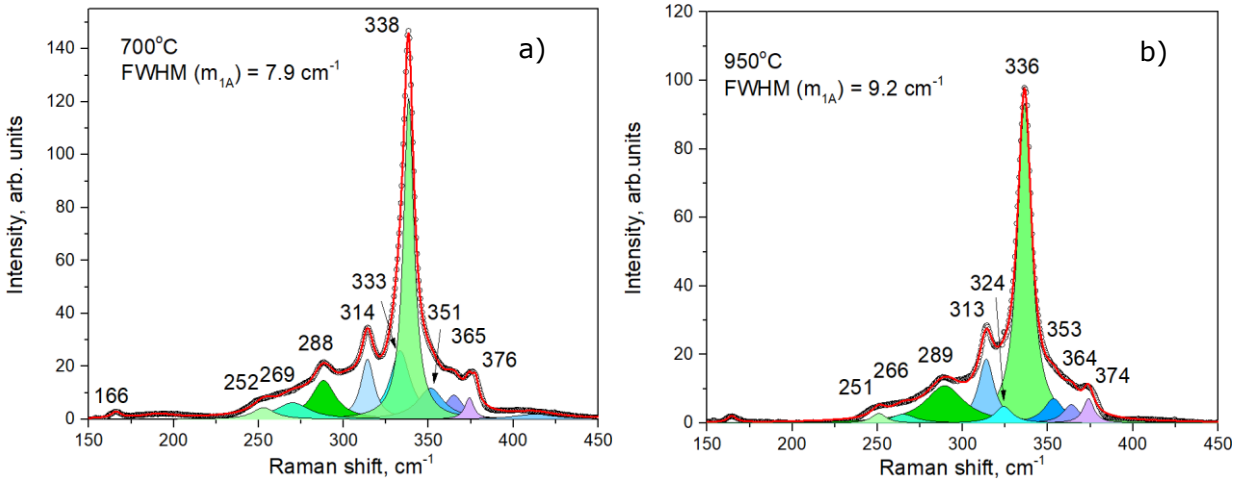

Figure 3.4 Raman spectra of the samples S700 (a) and S950 (b).

This broadening can be attributed to disordering within the crystal structure. In the Raman spectra of powders annealed at temperature 950 °C, it could be seen that in addition to the A_1 peak of kesterite (336 cm^{-1}), another proportionally significant peak becomes apparent at 313 cm^{-1}. This means that at higher temperatures, the synthesised kesterite CZTS starts to decompose (Figure 3.4 a, b). This peak corresponds to SnS_2, as it is one of the side products resulting from the decomposition of CZTS. Decomposition was also noticeable from temperature 700 °C and higher, resulting in the formation of SnS_2 and SnS as byproducts.

Previously, it has been studied that the disordering in the kesterite structures of CZTS is in accordance with a quantity measure (Q) derived from the Raman intensity, which involves Raman peaks of m_{2A} and m_{3A} (Figure 3.1) The used equation was:

$$Q = \frac{I(m_{2A})}{I(m_{3A})} \tag{3.1}$$

Consequently, this means that the higher the value of Q, the higher the order in the CZTS structures [24]. In this research, the Raman spectra of the peak m_{3A} was unstable and in some samples was not present at all. Due to this reason, the relation between Raman peaks m' and m_{1A} was studied instead. As could be seen on Figure 3.1, the peaks m_{1A}, m_{2A} and m_{3A} correspond to ~340 cm^{-1}, ~289 cm^{-1} and ~304 cm^{-1}, respectively.

As mentioned, due to the absence of the m_{3A} peak in some samples, focus was directed towards the ratio of the peaks m_{1A} and m'. The peak m' has been previously associated with disorder in the kesterite phase structure [28]. Therefore, to study the disorder in our samples, an equation was used to describe the relationship between the main peak of kesterite structure and the peak associated with the disordered structure of CZTS:

$$Q' = \frac{I(m')}{I(m_{3A})} \qquad (3.2).$$

With the definition of Q' being smaller for more ordered structures of the samples, Figure 3.5 shows the disorder of our samples based on Raman spectroscopy.

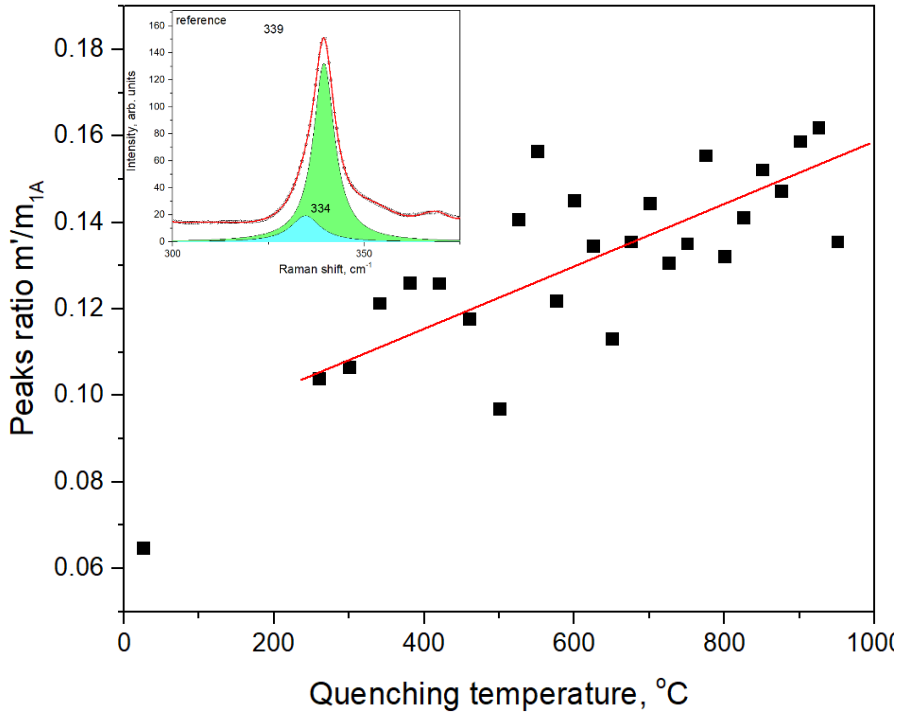

Temperature, °C	Q'
REF	0.065
260	0.104
300	0.107
340	0.121
380	0.126
420	0.126
460	0.118
500	0.097
525	0.141
550	0.157
575	0.122
600	0.145
625	0.135
650	0.113
675	0.136
700	0.144
725	0.131
750	0.135
775	0.156
800	0.132
825	0.141
850	0.152
875	0.147
900	0.159
925	0.162
950	0.136

Figure 3.5 Variation of Q' for CZTS samples post-annealed in different temperatures.

According to the peak ratio of m'/m_{1A}, it can be seen that the reference sample exhibits the lowest degree of disordering (Q'=0.06) among the samples, while the most disordered sample is S925 with Q'= 0.162 (Figure 3.5). The trend of the graph indicates that as the post-annealing temperature increases, the degree of disordering also increases. Referring to Figure 1.8, where disordering of crystalline material was described, it could be said that in our case, this disorder can also be represented in a graph based on the ratio of the peaks m'/m_{1A}. In

this experiment, the annealing time was not a measurable variable, as it was constant (t_{ann} = 15 minutes), and all applied annealing temperatures were over the critical temperature of kesterite CZTS (T_C = 260 °C), but different disordering degree was still influenced by temperature. Further research could focus on investigating the reversibility of the samples, as disordering should theoretically be reversible even at high temperatures. Another direction of research could involve varying the annealing time to understand the relationship between the duration of high temperature treatment and its effect on disordering.

3.2 Room-temperature photoluminescence spectroscopy

Room-temperature photoluminescence measurements were conducted for all the samples, with 10 measurements per sample. PL results were analysed using Origin 2015 and Origin 2018 software and fittings were done using Fityk program, employing the split Pseudo-Voigt function. PL studies have shown that kesterites have different recombination pathways. The biggest issues usually arise from defects within the material, like deep defects that facilitate recombination, and band-tails that limit the energy carrier's utilization. Very common antisite defects include Cu and Zn cations due to their low formation energy. Cu and Zn can easily substitute in the kesterite system due to their similar sizes and the reason that they don't differ much chemically. This swapping leads to antisite defects in the kesterite structure, like Cu_{Zn} and Zn_{Cu}, and other related complexes. These defects cause fluctuations in the electric charge and make the bands less uniform [43,44].

As expected, the reference sample showed an intense PL peak at 1.51 eV, which aligns with the band gap of the ordered kesterite CZTS (Figure 3.6). As the temperature increased, a reduction of the band gap was observed, and for sample S700, the PL peak had shifted by 0.07 eV (Figure 3.7a). This shift can be attributed to the Cu-Zn disorder, where copper and zinc atoms can interchangeably occupy the 2a, 2c, and 2d positions within the crystal structure [45]. As mentioned above, about 30% occurrence of disorder can result in a deviation of the band gap by ~100 meV. In this study, when comparing the reference sample to the sample annealed for 15 minutes at 700 °C, the observed shift was 70 meV. As shown in Figure 3.7b, at higher post-annealing temperatures, the CZTS structure started to decompose, leading to two distinct peaks in PL spectrum. Previous experiments using high-temperature X-ray diffraction have revealed a structural change in the material occurring around 900 °C. This change involves a transition from a tetragonal phase to a cubic phase. During the temperature

range between 866 °C and 883 °C, there is a mixture of both phases present. This transition is associated with the loss of ordered arrangement over long distances within the material's structure. As a result, the material progresses into a phase characterised by complete disorder in the arrangement of cations within the crystal lattice [46].

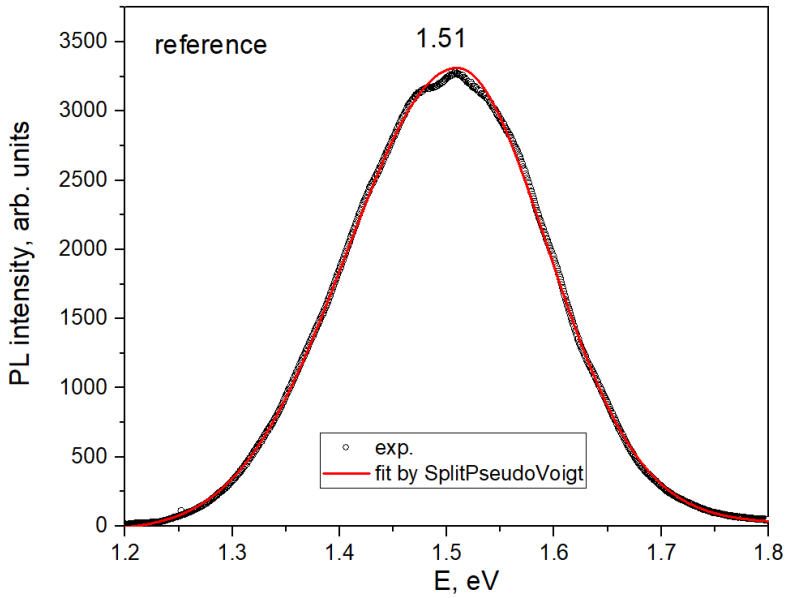

Figure 3.6 Fitted PL intensity of the reference sample.

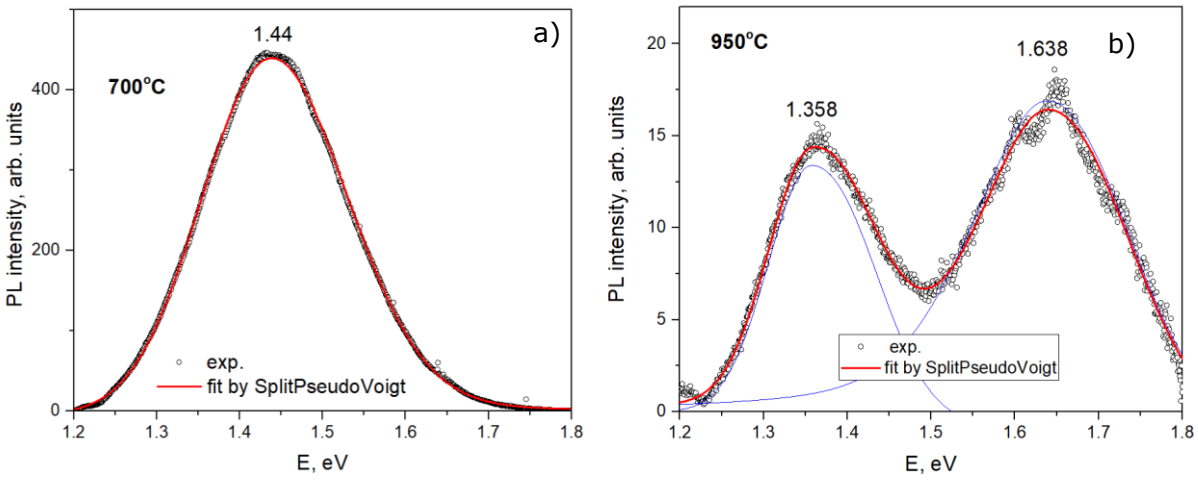

Figure 3.7 Fitted PL intensity of the sample S700 (a) and S950 (b).

Figure 3.8 solidifies the experiment's findings, demonstrating that at higher temperatures between 340 -825 °C for 15 minutes, the material becomes more disordered, accompanied by a decreasing in the position of the PL peak to ~1.43 eV. From the annealing temperature of

850 °C, the PL_{max} shifts to an even lower energy, and the powder heated at 925 °C or higher exhibits already two peaks at 1.36 and 1.64 eV in the PL spectrum.

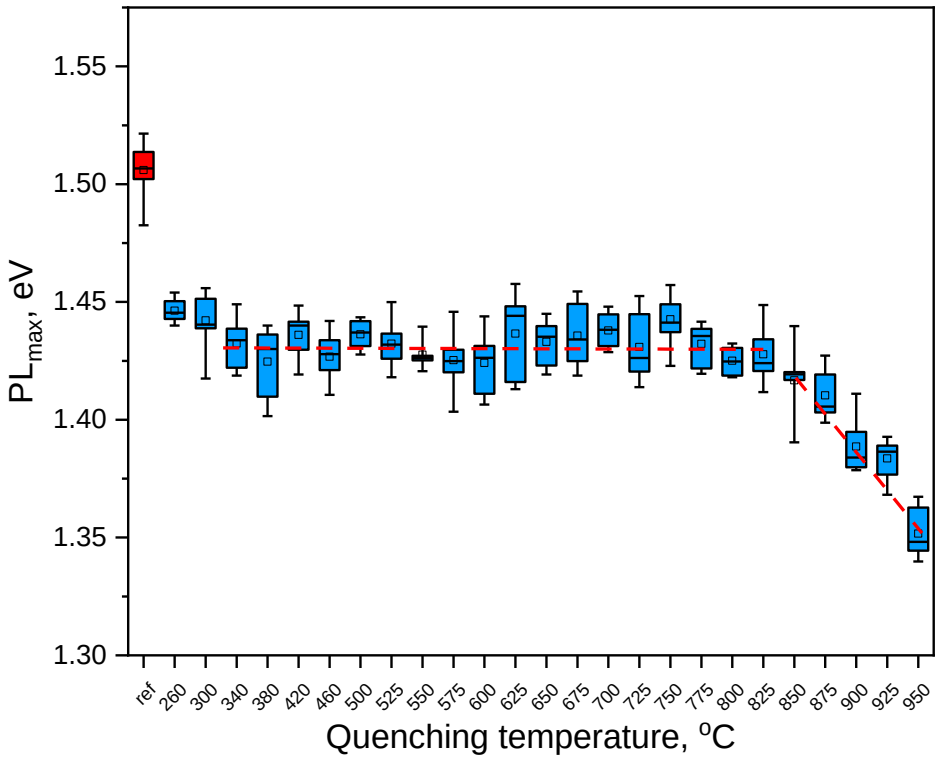

Figure 3.8 Box plot of the PL peak positions of samples post-annealed at different temperatures.

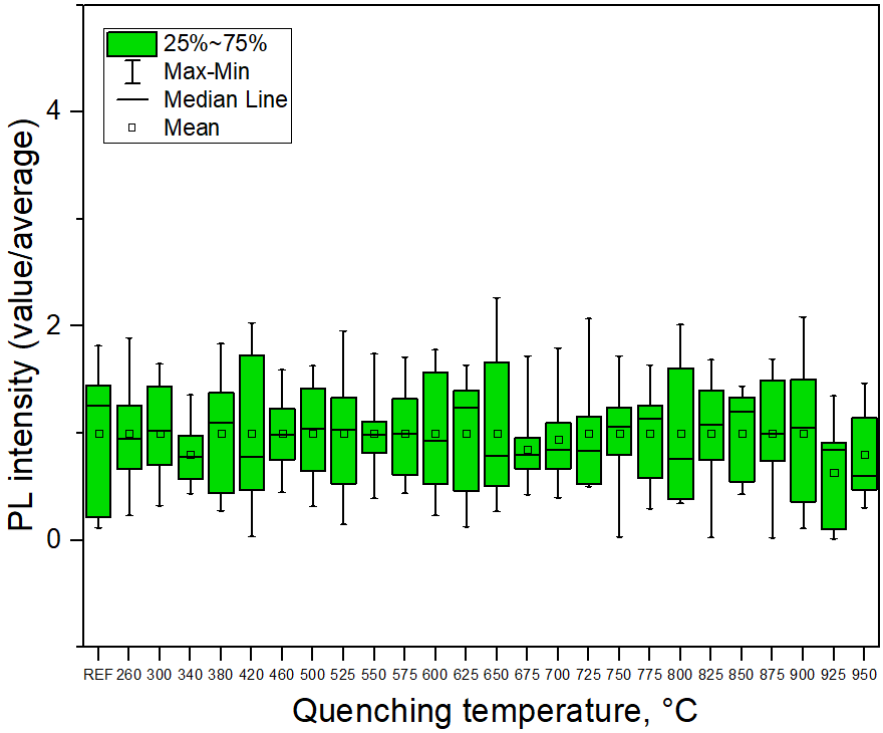

Figure 3.9 Box plot of relative deviation of PL peak intensities for all samples.

Figure 3.9 shows the measured PL intensities as a box plot graph, illustrating the grain-to-grain inhomogeneity. Different facets of CZTS monograins annealed at the same temperature exhibit considerable variability, as shown in the graph. The variability of PL intensities is presented by the relative deviation, which is calculated by dividing a measured PL intensity value by the average value. The relative deviation varies from ~0 to ~2. A possible reason could be the variations in disordering degree during the cooling process. This variability can lead to fluctuations, thereby influencing the output parameters of the produced cells.

3.3 Solar cell characteristics

To understand the effect of the disordering on the output parameters of solar cells, devices were produced using all the different samples as absorber layers in the monograin layer solar cell structures. All the samples' solar cell characteristics were measured, with a focus on V_{OC}, as this parameter can be most affected by the disordered structures of the material. Each solar cell had five measuring spots, with an active area of 0.045 cm^2. The J–V characteristics of the devices measured under illumination and obtained output parameters are presented as box plots in Figure 3.10. The mean value of efficiency for reference cell was 1.8% with V_{OC} = 650 mV, J_{SC} =9.1 mA/cm^2 and *FF* =37%. When the annealing temperature rises from 260 °C to 500 °C, the mean values of J_{SC} and *FF* increase to 11 mA/cm^2 and 55%, respectively, resulting in an increased mean efficiency of up to 3.7%. However, in this temperature range, V_{OC} decreases from 650 mV to 605 mV, indicating increased disordering in the CZTS structure. In the temperature range of 500 °C to 575 °C, all parameters decrease, resulting in an efficiency of 3.2%. This decreased efficiency can be caused by partial degradation of the CZTS surface due to insufficient vapor pressure in the ampoule to prevent it.

Then, from 600 °C to 700 °C, the enhancement of the three mentioned characteristics (J_{SC}, *FF*, and V_{OC}) is apparent again until decomposition starts again, and other phases (SnS, SnS_2) begin to develop. This means that intermediate temperatures above the T_C (260 °C), before the development of secondary phases, can have a positive effect on the output parameters of the solar cells. On Figure 3.10 it could be seen that all the output parameters were enhanced when the samples underwent post annealing process at temperatures between 260 to 825 °C.

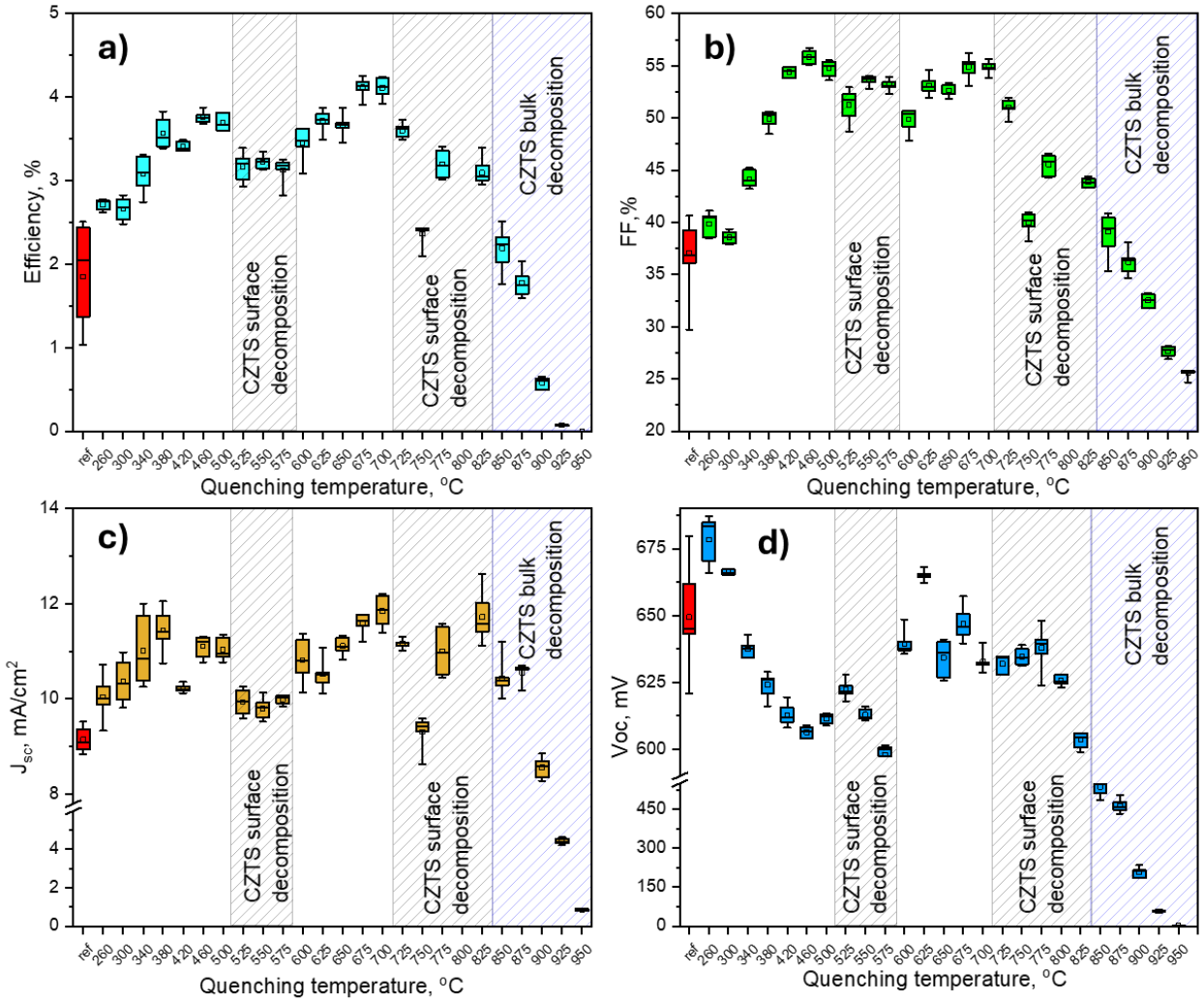

Figure 3.10 Output parameters of the produced solar cells.

Additionally, another comparison graph (Figure 3.11) was made to describe the relationship between PL_{max} and the respective V_{OC} measurements. Although the reference sample shows the highest maximum peak in the PL measurements, it does not have the highest V_{OC}. The highest V_{OC} belongs to the sample S260, with the annealing temperature being the critical temperature of CZTS. As seen in the graph, post-deposition annealing can have a positive effect on the V_{OC} of the solar cells, as samples S260, S300 and S625 all have higher V_{OC} values than the reference sample. This means that the disordered structures of CZTS is not the main reason for V_{OC}-deficit and can even enhance the output parameters of solar cells. This phenomenon definitely needs further studies, as this annealing experiment proved to be useful on increasing the parameters of produced solar cells.

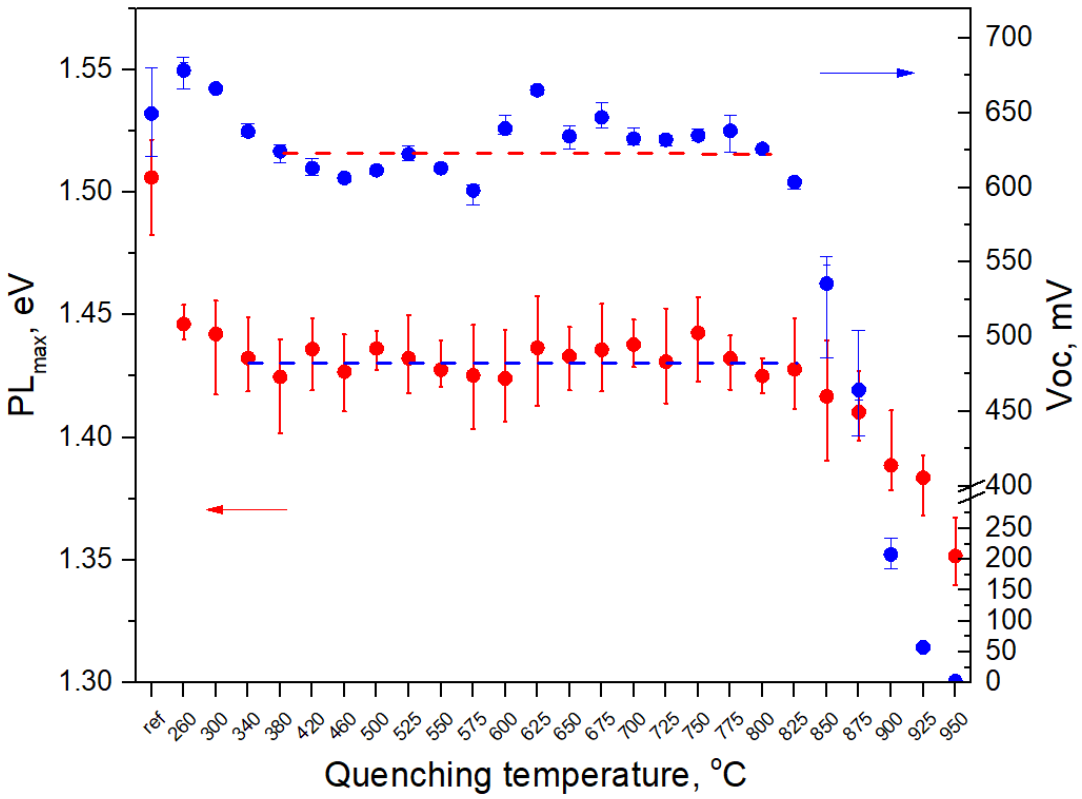

Figure 3.11. Graph comparing the measured PL_{max} to respective V_{OC} measurements.

As efficiency tends to be the most important parameter for solar cells, a table (Table 3.1) was created to illustrate the best samples of each annealing temperature based on efficiency. The best solar cell results were obtained with absorber materials annealed at temperatures between 625 °C and 700 °C, with efficiencies ranging from 3.9% to 4.24%, respectively.

Table 3.1 Output parameters of the solar cells produced in the research (chosen based on highest efficiency value).

Temperature, °C	***Voc*, mV**	***FF*, %**	***Jsc*, mA / cm^2**	**Eff., %**
REF	679.8	40.6	9.1	2.5
260	685.0	40.5	10.0	2.8
300	667.3	39.4	10.8	2.8
340	634.1	43.5	12.0	3.3
380	628.9	50.5	12.1	3.8
420	619.4	54.3	10.4	3.5
460	605.8	56.7	11.3	3.9
500	613.3	54.8	11.4	3.8
525	623.7	53.0	10.3	3.4
550	612.2	54.0	10.1	3.4
575	601.4	54.0	10.0	3.3

600	648.5	49.2	11.4	3.6
625	665.4	52.6	11.1	3.9
650	641.1	53.4	11.3	3.9
675	642.9	56.2	11.8	4.3
700	631.8	55.7	12.1	4.2
725	634.6	51.9	11.3	3.7
750	639.0	40.3	9.5	2.4
775	638.7	46.4	11.5	3.4
825	605.2	44.4	12.6	3.4
850	548.8	40.8	11.2	2.5
875	504.4	38.1	10.6	2.0
900	235.1	32.6	8.5	0.7
925	60.5	27.3	4.6	0.1
950	2.8	25.7	0.9	0.0

CONCLUSION

The aim of the present study was to induce various degrees of disorder in Cu_2ZnSnS_4 (CZTS) monograin powders by annealing them above the critical temperature (T_C=260 °C) between 260 °C and 950 °C, followed by rapid cooling in ice water. The effect of this disorder on the structural and optical properties of the CZTS crystal lattice was investigated using room temperature Raman spectroscopy and photoluminescence spectroscopy. In addition, powders with different interference levels were used as absorber material in monograin layer solar cells and their photovoltaic parameters were investigated.

Raman analysis showed that the main peak of disordered kesterite CZTS is at 336-338 cm^{-1}, consistent with established literature, with slight variations due to calibration differences.
The A1 peak in the Raman spectrum broadened from 6.9 cm^{-1} to ~9.2 cm^{-1} in samples subjected to higher annealing temperatures compared to the reference sample, indicating the increased degree of disordering within the crystal structure. The powders annealed at temperature higher than 700 °C, exhibited an additional peak at 313 cm^{-1} , which is signed to SnS_2 phase.

A new method to estimate the degree of disorder in CZTS monograin powders using the ratio of Raman peaks m' to m_{1A} was proposed. The peaks ratio m'/m_{1A} demonstrated a clear correlation between increasing post-annealing temperatures and the degree of disordering in CZTS samples. The reference sample (as grown) exhibited the lowest degree of disordering (Q'=0.06) among the samples, while the most disordered sample was S925 with Q'=0.162. This confirms that the degree of disordering increases with higher post-annealing temperature.

Room-temperature photoluminescence (PL) analysis revealed that the reference sample exhibited a broad PL peak at 1.51 eV. As the annealing temperature increased, the PL peak position notably shifted to lower energy values. Powders annealed between 340 -825 °C for 15 minutes exhibited increased disorder, resulting in a decrease in the PL peak position to ~1.43 eV. Annealing temperatures above 850 °C caused a further shift of PL_{max} to lower energy, and powders annealed at 925 °C or higher already exhibit two peaks at 1.36 and 1.64 eV in the PL spectrum.

The study also investigated the homogeneity of the powder facets by measuring the RT-PL spectra of at least 10 crystals. The intensities of the spectra varied considerably, possibly due to the short annealing time. This variability in intensities may also be due to changes in

radiative and non-radiative recombination during the cooling process, potentially leading to fluctuations that affected the performance of the produced cells.

The research additionally explored the impact of disordering in CZTS powders on the output parameters of monograin layer solar cells. The mean value of efficiency of the reference cell was 1.8%, with V_{OC} = 650 mV, J_{SC} = 9.1 mA/cm², and *FF* = 37%. As the annealing temperature was increased from 260 °C to 500 °C, the mean values of J_{SC} and *FF* increased to 11 mA/cm² and 55%, respectively, resulting in an increased efficiency up to 3.7%. However, in this temperature range, V_{OC} decreased from 650 mV to 605 mV, indicating increased disordering in the CZTS structure. In the temperature range of 500 °C to 575 °C, all parameters decreased, resulting in an efficiency of 3.2%. This decrease in efficiency may be attributed to partial degradation of the CZTS surface due to insufficient vapor pressure in the ampoule to prevent it. Between 600 °C and 700 °C, an enhancement in characteristics was observed until further decomposition occurred. As also Raman analysis revealed, annealing above 700 °C, peaks of secondary phases such as SnS_2 appear, indicating surface decomposition. At temperatures above 825 °C, the CZTS material begins to decompose also in the bulk. This decomposition is reflected also in the output parameters. The average efficiency decreases from 3.6% to 3.1% when CZTS powders were annealed at 725-825 °C, and at higher temperatures, the output parameters of the solar cell drop to nearly zero.
In conclusion, CZTS annealing above the critical temperature (T_C) improved the efficiency of solar cells, but temperatures that cause surface and bulk decomposition should be avoided.

Future research should explore the reversibility of this disordering at high temperatures and investigate the effects of different annealing durations. This could provide a deeper understanding of the thermal stability and structural stability of CZTS, which is crucial for optimizing its use in photovoltaics. These results highlight the critical influence of thermal treatment on the structural and electronic properties of CZTS, suggesting further research on optimizing annealing processes to mitigate defects and enhance device performance.

SUMMARY

The global energy demand is constantly increasing as the population is rapidly growing and global fossil fuel reserves are steadily decreasing. These factors significantly influence the ways we will obtain energy in the future. Taking this into consideration, the world should focus on alternative energy sources. Supporting this is the fact that the European Union, in agreement with its member states, has coordinated the so-called Green Deal to make Europe a climate-neutral region by 2050. I believe that with this thesis, I can contribute to this. Solar panels are certainly a step in the right direction, but there is definitely room for development in this field, and one of the directions of development is thin-film solar cells.

Within this thesis, 26 samples of kesterite structure CZTS were produced. The samples differed in terms of the degree of disorder in the crystal structure. Different disordering degrees in the structures were achieved by varying post-deposition annealing temperatures, ranging from 260 °C to 950 °C. All the samples were annealed for 15 minutes and then quenched in ice water.

One of the objectives of the thesis was to study how does the Cu-Zn disordering in the crystal structure changes the optical and structural properties, using Raman spectroscopy and photoluminescence spectroscopy. Raman spectroscopy confirmed an increase in degrees of disorder with higher post-deposition annealing temperatures. This fact was also supported by room-temperature photoluminescence studies, which showed the PL peak shifting towards lower energy values. Analysis of the room-temperature photoluminescence measurements also revealed inhomogeneity of the grains in similar samples, which could negatively impact the performance of the produced solar cells.
For the second objective of the thesis, monograin layer solar cells were produced using all the samples as absorber layers to study the effect of the disordered structures on the output parameters of the solar cells. This approach proved to be effective, as some samples with higher annealing temperatures (and a higher degree of disorder) exhibited better output parameters than the reference sample.

These results provide a basis for further and deeper study of kesterite CZTS as an absorber layer in solar cell structure. The research and experiments demonstrated that disordered structures of the absorber layer crystals of kesterite CZTS can positively affect the output parameters of solar cells. This indicates that the disorder in crystal structure is not the main

reason for open-circuit voltage deficit of kesterite based solar cells, encouraging more detailed exploration of this material for photovoltaic applications.

LIST OF REFERENCES

[1] The European Green Deal - European Commission, (n.d.). https://commission.europa.eu/strategy-and-policy/priorities-2019-2024/european-green-deal_en (accessed May 2, 2024).

[2] E. Union, Environment : EU ban on hazardous substances in electrical and electronic products takes effect, Environ. EU Ban Hazard. Subst. Electr. Electron. Prod. Tak. Eff. (2006) 1–2. http://europa.eu/rapid/press-release_IP-06-903_en.htm?locale=en.

[3] S. Brown, D. Jones, European Electricity Review 2024 | Ember, (2024). https://ember-climate.org/insights/research/european-electricity-review-2024/#supporting-material (accessed April 29, 2024).

[4] B. Zaidi, Introductory Chapter: Introduction to Photovoltaic Effect, in: Sol. Panels Photovolt. Mater., InTech, 2018. https://doi.org/10.5772/intechopen.74389.

[5] Photovoltaic effect | Solar Energy Conversion, Photons & Electrons | Britannica, (n.d.). https://www.britannica.com/science/photovoltaic-effect (accessed February 20, 2024).

[6] Best Research-Cell Efficiency Chart | Photovoltaic Research | NREL, (n.d.). https://www.nrel.gov/pv/cell-efficiency.html (accessed February 20, 2024).

[7] Quadruple Junction Solar Cell with 47.6 % Conversion Efficiency under Concentration, (n.d.). https://publica.fraunhofer.de/entities/publication/e2ce1921-d7b8-41df-a037-2d82e399d015/details (accessed February 20, 2024).

[8] J. Pastuszak, P. Węgierek, Photovoltaic Cell Generations and Current Research Directions for Their Development, Materials (Basel). 15 (2022). https://doi.org/10.3390/MA15165542.

[9] Semiconductors | Properties, Characteristics & Use, (n.d.). https://www.electricity-magnetism.org/semiconductors/ (accessed February 20, 2024).

[10] Difference Between Conductor, Semiconductor and Insulator, (n.d.). https://www.electricaltechnology.org/2019/10/difference-between-conductor-semiconductor-insulator.html (accessed February 26, 2024).

[11] T. Soga, Fundamentals of Solar Cell, Nanostructured Mater. Sol. Energy Convers. (2006) 3–43. https://doi.org/10.1016/B978-044452844-5/50002-0.

[12] T. Markvart, L. Castañer, Principles of Solar Cell Operation, Pract. Handb. Photovoltaics Fundam. Appl. (2003) 71–93. https://doi.org/10.1016/B978-185617390-2/50005-2.

[13] A.-M. Mandong, Design and simulation of single, double, and multi-layer antireflection coating for crystalline silicon solar cell, (2019) 9707–9710. https://www.mendeley.com/catalogue/6939b94e-2844-38b4-9770-fa71d677f849/?utm_source=desktop&utm_medium=1.19.8&utm_campaign=open_catalog&userDocumentId=%7B05ae71d7-3206-389f-abec-55696daef387%7D (accessed February 28, 2024).

[14] M. Shahiduzzaman, M.I. Hossain, M. Akhtaruzzaman, M. Nakano, M. Karakawa, J.M. Nunzi, T. Taima, Organometal halide perovskite photovoltaics, Elsevier, 2021. https://doi.org/10.1016/B978-0-323-85529-7.00007-4.

[15] S. Enayati Maklavani, S. Mohammadnejad, Enhancing the open-circuit voltage and efficiency of CZTS thin-film solar cells via band-offset engineering, Opt. Quantum Electron. 52 (2020) 1–22. https://doi.org/10.1007/S11082-019-2180-6/FIGURES/11.

[16] M. Kauk-Kuusik, K. Timmo, M. Pilvet, K. Muska, M. Danilson, J. Krustok, R. Josepson, V. Mikli, M. Grossberg-Kuusk, Cu 2 ZnSnS 4 monograin layer solar cells for flexible photovoltaic applications, J. Mater. Chem. A. 11 (2023) 23640–23652. https://doi.org/10.1039/D3TA04541B.

[17] A. Wang, M. He, M.A. Green, K. Sun, X. Hao, A Critical Review on the Progress of Kesterite Solar Cells: Current Strategies and Insights, Adv. Energy Mater. 13 (2023) 2203046. https://doi.org/10.1002/AENM.202203046.

[18] N. Kattan, B. Hou, D.J. Fermín, D. Cherns, Crystal structure and defects visualization of Cu2ZnSnS4 nanoparticles employing transmission electron microscopy and electron diffraction, Appl. Mater. Today. 1 (2015) 52–59. https://doi.org/10.1016/J.APMT.2015.08.004.

[19] A. Ritscher, M. Hoelzel, M. Lerch, The order-disorder transition in Cu2ZnSnS4 – A neutron scattering investigation, J. Solid State Chem. 238 (2016) 68–73.

https://doi.org/10.1016/J.JSSC.2016.03.013.

[20] K. Rudisch, Defect Engineering in Kesterite Materials for Thin Film Solar Cells, (2020). http://www.diva-portal.org/smash/record.jsf?dswid=6702&pid=diva2%3A1417588&c=1&searchType=SIMPLE&language=en&query=KATHARINA+RUDISCH&af=%5B%22publicationTypeCode%3AcomprehensiveDoctoralThesis%22%5D&aq=%5B%5B%5D%5D&aq2=%5B%5B%5D%5D&aqe=%5B%5D&noOfRows=50&s (accessed March 2, 2024).

[21] S. Schorr, The crystal structure of kesterite type compounds: A neutron and X-ray diffraction study, Sol. Energy Mater. Sol. Cells. 95 (2011) 1482–1488. https://doi.org/10.1016/J.SOLMAT.2011.01.002.

[22] K. Timmo, M. Kauk-Kuusik, M. Pilvet, T. Raadik, M. Altosaar, M. Danilson, M. Grossberg, J. Raudoja, K. Ernits, Influence of order-disorder in Cu2ZnSnS4 powders on the performance of monograin layer solar cells, Thin Solid Films. 633 (2017) 122–126. https://doi.org/10.1016/J.TSF.2016.10.017.

[23] M. He, C. Yan, J. Li, M.P. Suryawanshi, J. Kim, M.A. Green, X. Hao, Kesterite Solar Cells: Insights into Current Strategies and Challenges, Adv. Sci. 8 (2021) 2004313. https://doi.org/10.1002/ADVS.202004313.

[24] J.J.S. Scragg, L. Choubrac, A. Lafond, T. Ericson, C. Platzer-Björkman, A low-temperature order-disorder transition in Cu2ZnSnS4 thin films, Appl. Phys. Lett. 104 (2014) 41911. https://doi.org/10.1063/1.4863685/379659.

[25] G. Rey, A. Redinger, J. Sendler, T.P. Weiss, M. Thevenin, M. Guennou, B. El Adib, S. Siebentritt, The band gap of Cu2ZnSnSe4: Effect of order-disorder, Appl. Phys. Lett. 105 (2014) 112106. https://doi.org/10.1063/1.4896315/133057.

[26] W.L. Bragg, E.J. Williams, The effect of thermal agitation on atomic arrangement in alloys, Proc. R. Soc. London. Ser. A, Contain. Pap. a Math. Phys. Character. 145 (1934) 699–730. https://doi.org/10.1098/RSPA.1934.0132.

[27] P. Mangelis, P. Vaqueiro, R.I. Smith, A. V. Powell, The onset of copper-ion mobility and the electronic transition in the kesterite Cu2ZnGeSe4, J. Mater. Chem. A. 9 (2021) 27493–27502. https://doi.org/10.1039/D1TA08642A.

[28] M. Grossberg, J. Krustok, J. Raudoja, T. Raadik, The role of structural properties on

deep defect states in Cu 2ZnSnS 4 studied by photoluminescence spectroscopy, Appl. Phys. Lett. 101 (2012). https://doi.org/10.1063/1.4750249.

[29] K. Timmo, M. Pilvet, K. Muska, M. Altosaar, V. Mikli, R. Kaupmees, R. Josepson, J. Krustok, M. Grossberg-Kuusk, M. Kauk-Kuusik, Influence of alkali iodide fluxes on Cu2ZnSnS4 monograin powder properties and performance of solar cells, Mater. Adv. 4 (2023) 4509–4519. https://doi.org/10.1039/D3MA00444A.

[30] M. Kauk-Kuusik, X. Li, M. Pilvet, K. Timmo, M. Grossberg, T. Raadik, M. Danilson, V. Mikli, M. Altosaar, J. Krustok, J. Raudoja, Study of Cu2CdGeSe4 monograin powders synthesized by molten salt method for photovoltaic applications, Thin Solid Films. 666 (2018) 15–19. https://doi.org/10.1016/J.TSF.2018.09.025.

[31] K. Timmo, M. Kauk-Kuusik, M. Pilvet, M. Altosaar, M. Grossberg, M. Danilson, R. Kaupmees, V. Mikli, J. Raudoja, T. Varema, Cu(In,Ga)Se2 monograin powders with different Ga content for solar cells, Sol. Energy. 176 (2018) 648–655. https://doi.org/10.1016/J.SOLENER.2018.10.078.

[32] F. Ghisani, K. Timmo, M. Altosaar, J. Raudoja, V. Mikli, M. Pilvet, M. Kauk-Kuusik, M. Grossberg, Synthesis and characterization of tetrahedrite Cu10Cd2Sb4S13 monograin material for photovoltaic application, Mater. Sci. Semicond. Process. 110 (2020) 104973. https://doi.org/10.1016/J.MSSP.2020.104973.

[33] A. Pan, X. Zhu, Optoelectronic properties of semiconductor nanowires, in: Semicond. Nanowires, Elsevier, 2015: pp. 327–363. https://doi.org/10.1016/B978-1-78242-253-2.00012-8.

[34] W. Fuhs, ZnO Window Layers for Solar Cells, Zinc Oxide — A Mater. Micro-Optoelectron. Appl. (2005) 197–209. https://doi.org/10.1007/1-4020-3475-x_17.

[35] K. Ellmer, R. Wendt, R. Cebulla, ZnO/ZnO:Al window and contact layer for thin film solar cells: high rate deposition by simultaneous rf and dc magnetron sputtering, Conf. Rec. IEEE Photovolt. Spec. Conf. (1996) 851–854. https://doi.org/10.1109/pvsc.1996.564269.

[36] J. Krustok, Raman spektroskoopia, (2020).

[37] What is Raman Spectroscopy? - HORIBA, (n.d.). https://www.horiba.com/int/scientific/technologies/raman-imaging-and-

spectroscopy/raman-spectroscopy/ (accessed April 24, 2024).

[38] Photoluminescence of Semiconductors, (n.d.). https://www.horiba.com/fra/scientific/applications/energy/pages/photoluminescence-of-semiconductors/ (accessed April 29, 2024).

[39] Photoluminescence - an overview | ScienceDirect Topics, (n.d.). https://www.sciencedirect.com/topics/materials-science/photoluminescence (accessed April 29, 2024).

[40] TalTech Päikeseenergeetika materjalide teaduslabor, Päikesepatarei volt-amper karakteristiku mõõtmine, 2019.

[41] K. Mertens, Photovoltaics: Fundamentals, Technology and Practice, 2014.

[42] A. Khare, B. Himmetoglu, M. Johnson, D.J. Norris, M. Cococcioni, E.S. Aydil, Calculation of the lattice dynamics and Raman spectra of copper zinc tin chalcogenides and comparison to experiments, J. Appl. Phys. 111 (2012) 83707. https://doi.org/10.1063/1.4704191/923997.

[43] M. Grossberg, J. Krustok, C.J. Hages, D.M. Bishop, O. Gunawan, R. Scheer, S.M. Lyam, H. Hempel, S. Levcenco, T. Unold, The electrical and optical properties of kesterites, J. Phys. Energy. 1 (2019) 044002. https://doi.org/10.1088/2515-7655/AB29A0.

[44] G. Rey, G. Larramona, S. Bourdais, C. Choné, B. Delatouche, A. Jacob, G. Dennler, S. Siebentritt, On the origin of band-tails in kesterite, Sol. Energy Mater. Sol. Cells. 179 (2018) 142–151. https://doi.org/10.1016/J.SOLMAT.2017.11.005.

[45] Y.F. Zheng, J.H. Yang, X.G. Gong, Cu-Zn disorder in stoichiometric and non-stoichiometric Cu2ZnSnS4/Cu2ZnSnSe4, AIP Adv. 9 (2019) 35248. https://doi.org/10.1063/1.5090804/1077142.

[46] S.P. Ramkumar, A. Miglio, M.J. Van Setten, D. Waroquiers, G. Hautier, G.M. Rignanese, Insights into cation disorder and phase transitions in CZTS from a first-principles approach, Phys. Rev. Mater. 2 (2018) 085403. https://doi.org/10.1103/PHYSREVMATERIALS.2.085403/FIGURES/5/MEDIUM.